Sub-threshold J/ψ Photoproduction

Claire Alexandra Lee

A dissertation submitted to the Faculty of Science,
University of the Witwatersrand, Johannesburg,
in fulfillment of the requirements for the
degree of Master of Science.

Johannesburg, 2009

Candidate's Declaration

I declare that this dissertation is my own, unaided work. It is being submitted for the degree of Master of Science in the University of the Witwatersrand, Johannesburg. It has not been submitted before for any degree or examination at any other University.

_____

Claire A. Lee (candidate)

_____ day of _____ 2009

Abstract

Jefferson Lab experiment E03-008 aimed to measure the J/ψ photoproduction cross section at energies sub-threshold to a free nucleon. Prior data extended only to just above threshold; the closest-to-threshold measurements come from Cornell and SLAC and provide data in the 9.3 to 21 GeV region. For E03-008, a mixed real and quasi-real bremsstrahlung photon beam with an endpoint energy of 5.76 GeV incident on a solid carbon target was used, allowing measurement for the first time in the sub-threshold region. The sub-threshold energy of the beam required momentum contributions from the nucleon target to bring the energy of the reaction up to threshold, thus providing an opportunity to probe higher order nucleon correlations within the nucleus as well as exotic mechanisms that may enhance the cross section. The aim of the analysis was to study the parametrization of the cross section near threshold and comment on the predictions made by theoretical models of the J/ψ photoproduction reaction mechanism. No J/ψ events were observed, a result which is consistent with predictions under the assumption of quasi-free photoproduction, and places restictions on exotic mechanisms that would strongly enhance quasi-free production.

Acknowledgements

First and foremost I must thank my parents, Greg and Karen Gray, for raising me to value the quest for knowledge, instilling in me a desire to learn, and giving me the opportunities to do so. Besides love I think this is the most valuable thing you can give a child, and they certainly excelled at both. To my husband, Chris, who has stood beside and supported me throughout the years, and put up with more than his fair share of frustration, thank you for being there for me. You make it all worthwhile.

A special thanks go to my advisors, Simon Connell (University of Johannesburg) and Peter Bosted (Jefferson Lab), for the advice and patience they have had over the years, and for the opportunity I had to work on this experiment. Their insights and discussions have taught me so much, and I count myself very lucky to have been able to work with such great physicists. Extra thanks must go to Simon for the support and encouragement he continued to give me and everyone around him, even when he sometimes needed it the most. Thanks also to my Wits supervisor Robert de Mello Koch, who often inspired me with his passion for physics, and was never too busy for a chat when I bumped into him getting coffee in the mornings.

To my friend and fellow JLab-ee, Mark Dalton, a very special thanks. It was with Mark's help that I was first immersed in the Hall C experiments, learning the ropes on a project in my fourth (Honours) year. Mark has traveled with me twice to Jefferson Lab, answered countless questions on just about everything Hall C- and ROOT-related, and with whom I have shared much laughter. He was often the first person I would turn to when I ran into a problem, and our friendship will always be treasured. A sincere thanks goes to Sergio Ballestrero, for his astounding computing and analysis skills and tireless help, and who has also become my friend over the years.

I joined the experiment in the middle of data-taking at the end of November 2004. Thanks to Simon Connell for the opportunity, and all his help in organising the trip to Jefferson Lab in less than two weeks. Thanks also to all those involved in the conception, proposal, preparation and running of this experiment, mentioned in the paper (see Appendix D) and without whom the successful run would not have been possible. A special thanks must go to Jim Dunne, for his help, insights and work on the analysis.

I would like to thank the members of the PSI Group whom I have met and worked alongside over the years, specifically Mark Dalton, Sergio Ballestrero, Georgie Mbianda Njencheu, Doomnull Attah Unwuchola and Winile Sibande. It was great to be part of such a diverse group of people, working on a diverse set of experiments, and a comfort all being in it together. The camaraderie and support for each other, especially at the yearly South African Institute of Physics conferences, will always be valued.

Finally, I would like to acknowledge the National Research Foundation (NRF) for their funding through the Grantholder Bursary, and their Mobility Grant and Simon's Research Grant through which my trips overseas were made possible. My expenses locally at Jefferson Lab were covered by Hall C, for which I am also very grateful.

Contents

List of Figures

List of Tables

Chapter 1

Introduction

One of the main goals of nuclear physics is to understand just how a nucleus differs from a loosely bound system of quasi-independent nucleons, as in experiments it is often necessary to use a nuclear target instead of the preferred free nucleon target due to the relative difficulty of producing a free nucleon. However, spatially close nucleons correspond to rare high momentum components of the single particle wave function and at these close distance scales many interesting configurations can arise, producing contributions over and above those from single-particle scattering.

One way to probe the high momentum components is to investigate reactions on a nucleus that would be sub-threshold to reactions from a free nucleon, thus relying on the intrinsic nucleon momentum to provide the extra energy to bring the reaction to threshold. One of the cleanest such reactions is the photoproduction of the J/ψ, since the charm content of the nucleon is very small compared to that of the lighter quarks. In this case, the quark-interchange mechanism is absent (unlike with light meson photoproduction

where the quark content can originate in the nucleon) so the reaction proceeds via gluon exchange to conserve colour. Also, due to the heavy mass of the charm quark (1.3 GeV), sub-threshold photons would be unable to excite the higher charmonium states that decay to the J/ψ, leaving us with only a single direct J/ψ photoproduction mechanism. The goal of this research was to obtain the sub-threshold photoproduction cross section of the J/ψ via experiment, therefore probing the production mechanisms at short distance scales that could enhance the quasi-free production.

1.1 Overview of the Experiment

The data for this experiment was taken in November/December 2004 at the Thomas Jefferson National Accelerator Facility (Jefferson Lab) in Virginia, USA. The experiment, "E03-008: Sub-threshold J/ψ Photoproduction" ran with a 5.7 GeV electron beam incident on a solid carbon target to produce real photons via Bremsstrahlung. The aim was to photoproduce J/ψ mesons through an interaction with the carbon nucleons and detect the J/ψ's via their decay to lepton pairs. Using photons of endpoint energy 5.7 GeV, we obtained the first measurements for J/ψ photoproduction with sub-threshold energies.

1.2 Structure of the Dissertation

In Chapter 2 we explore the photoproduction mechanism for the J/ψ, and look at the necessary considerations for probing the reaction at sub-threshold energies. In Chapter 3 we examine the current data for near-threshold photo-

production. Chapter 3 also includes a discussion of the J/ψ photoproduction cross section models used by the previous experiments, and the method used for modeling quasi-free production in this research.

In Chapter 4 we review the apparatus used for the experimental measurement. We note the setup of the Jefferson Lab accelerator, and discuss the spectrometers and their detector elements used for the measurements. Chapter 5 describes the checks that were done as verification that the spectrometer and analysis systems were functioning as they should, as well as the results of the J/ψ photoproduction data. Calibration measurements were also taken, checking the spectrometer settings and resolutions and making sure we see the expected peaks from known resonances. We also discuss the method used for particle identification in the spectrometers.

Finally, Chapter 6 describes the various cross section models investigated, and shows the predictions generated thereof. We discuss the outcomes of these predictions in relation to the present experiment, and the constraints drawn on the models as a result.

Chapter 2

J/ψ Photoproduction

The J/ψ meson is the first excited state of charmonium, a bound state of a charm quark-antiquark pair. In the case of J/ψ photoproduction, a real (or very low q^2 virtual) photon fluctuates into a charm-anticharm pair, which is then brought on-shell through interaction with a nucleon. While the J/ψ is a common particle to observe experimentally, this interaction mechanism is not well understood and is dependent on the energy of the incoming photon.

In the lab frame, the threshold energy for production of the J/ψ on a nucleon is $(m + M_{J/\psi})^2 = 16.3$ GeV^2, where m is the nucleon mass and $M_{J/\psi}$ is the mass of the J/ψ (3.1 GeV). The invariant mass of the photon-nucleon system is given by $s = m^2 + 2mk$. For s to be above the threshold value for J/ψ production, a photon threshold energy of $k_{th} = 8.2$ GeV is required.

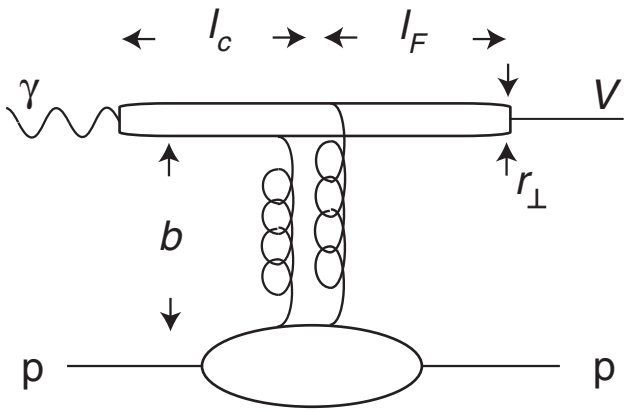

Figure 2.1: Characteristic length scales in J/ψ photoproduction on a proton near threshold. [1]

2.1 J/ψ Photoproduction from a Nucleon

Above but near the photon energy threshold, J/ψ production occurs in a small interaction volume (Fig. 2.1) due to the large mass of the charm quark ($m_c \approx 1.5$ GeV). The longitudinal distance the photon-$c\overline{c}$ fluctuation travels is given by [1]

$$l_c \cong \frac{2k_{lab}}{4m_c^2} = 0.36 \text{ fm} \tag{2.1}$$

with a transverse size $r_\perp \sim \frac{1}{m_c} \sim 0.13$ fm. At threshold the minimum momentum transfer required is large, $t_{min} \sim 1.7$ GeV^2, so the available production energy cannot be wasted. Thus the three valence quarks of the target must interact coherently with the heavy $c\overline{c}$ quarks within the small impact distance $b \sim \frac{1}{m_c} \sim 0.13$ fm and during their proper creation time $\frac{1}{m_c}$ for J/ψ production to take place. The effective proton radius also decreases with photon energy [2, 3] reaching $r_{\perp p}^2 \sim \frac{1}{m_c^2}$ at threshold.

After the interaction with the nucleon, the $c\overline{c}$ pair evolves into a J/ψ within the formation length l_F, related to the reversed distance between low-energy levels of the $c\overline{c}$ system, multiplied by the Lorentz factor [4, 5]:

$$l_F \cong \frac{2}{m_{\psi'} - m_{J/\psi}} [\frac{E_{J/\psi}}{2m_c}] \cong 0.22 \text{ fm } k/\text{GeV} \tag{2.2}$$

This length is approximately 1 fm, of the order of the size of a nucleon, allowing for determination of the J/ψ cross section on a single nucleon rather than on the nucleus as a whole.

2.2 Sub-threshold Photoproduction Kinematics

For photon energies below the threshold value of 8.2 GeV, the nucleon is required to contribute the extra energy needed to bring the center of mass energy squared s of the photon-nucleon system up to threshold. In the quasi-free picture, for J/ψ photoproduction off a single nucleon in a nucleus, the nucleon three-momentum P_m must be anti-parallel to the photon direction z to contribute to the invariant mass of the system. Thus, for a given photon energy k

$$s = (k + m - E_m)^2 - k^2 - P_m^2 - 2\vec{k} \cdot \vec{P}_m. \tag{2.3}$$

where E_m is the missing energy of the photon-nucleon system and must be greater than zero. Clearly, the larger the value of E_m, the smaller the value of s becomes at fixed P_m, so we have an upper bound on values of E_m that are kinematically allowed for J/ψ photoproduction. Furthermore, the minimum nucleon momentum P_m must increase as the photon energy k decreases, to

keep the energy of the system above threshold.

For a photon energy of 8 GeV, just below threshold, the minimum nucleon momentum required is just 0.05 GeV. When the photon energy is reduced to 6 GeV, the minimum momentum required increases to 0.35 GeV, and for 4 GeV photons, it is 1.15 GeV. For nucleon momenta larger than 0.35 GeV, this is the region where few-nucleon short-range correlations and other effects are known to be important [6, 7]. This is well suited to the Electron Beam Facility at Jefferson Lab with a maximum electron beam energy of 5.76 GeV at the time of this experiment, providing real and quasi-real photons by Bremsstrahlung. The determination of the J/ψ cross section in the 8-11 GeV region will be possible with the future Jefferson Lab 12 GeV upgrade [8, 9].

2.2.1 The High $\vec{P}_m$ Region

As mentioned above, the high $\vec{P}_m$ region, for nucleon momenta above 0.35 GeV, is where few-nucleon short-range correlations, hidden colour configurations, and other short-range effects play a significant role, possibly enhancing the yield compared to that predicted by a simple quasi-free model. In the model employed by [1], this could correspond to contributions from 3-gluon exchange, above the minimal 2-gluon exchange contribution for a J/ψ colour singlet final state.

Another way to see the effect of short-range correlations is in the photon thresholds for J/ψ production on other targets: for a deuteron at rest, the photon threshold is 5.7 GeV, and 4.8 GeV for tritium or ^{3}He targets at rest.

In the case of threshold charm production on a deuteron, all configurations of the six valence quarks are involved at the short distance scale $\frac{1}{m_c}$. Thus the second contribution comes from the coupling of the exchanged gluons to colour-octet 3-quark clusters, revealing the "hidden-colour" part of the nuclear wave function [10, 11, 12]. This contribution is thought to be flatter in its momentum distribution, as the two nucleons have to recombine, each at the momentum transfer $\frac{t}{4}$ [13, 14]. This contribution could be important in the sub-threshold region for J/ψ production, since each of the two exchanged gluons could have a lower momentum fraction than if they originate from the same nucleon. In any case, two- and three-nucleon correlations in the carbon nucleus are thus needed to kinematically permit J/ψ photoproduction at photon energies below 6 GeV.

2.3 Relation to Sub-threshold Hadroproduction

The method of selecting particle production on a nucleus at energies that would be sub-threshold to production from a free nucleon is not limited to charmonium. It has been observed for antiproton ($\overline{p}$) production in p-nucleus (pA) and nucleus-nucleus (AA) collisions of various nuclei [15, 16, 17], and kaon production from pA collisions [18], that production occurs at significantly lower energies than would be kinematically possible for scattering off a free nucleon. At these lower energies, the momentum required for a free nucleon is around 850 MeV [16]. The experimental data can be compared with model predictions calculated using internal nucleon momentum distri-

butions; for pA collisions the predictions give excellent agreement with the data. For AA collisions, however, the predictions underestimate the data by about three orders of magnitude [19].

At least two qualitatively different scenarios are available for sub-threshold $\overline{p}$ production [2]. In the first scenario, the projectile scatters off an area of high energy density, or local "hot spot". In this case the kinematic threshold is lowered due to the high effective mass of the "hot spot". In the second scenario, however, the momentum is not transferred locally but rather accumulated in an extended longitudinal region as the projectile travels through the nucleus.

Sub-threshold photoproduction of charmonium can help to identify the correct reaction mechanism. At and below the charm threshold the photon is point-like and is therefore a clean probe of target substructure, effects due to the shrinking size of a hadron probe near threshold are therefore eliminated. Also, the $c\overline{c}$ pair is created locally within the proper time $\frac{1}{m_c}$, so the extended region scenario is not available as a reaction mechanism for this process. A strong sub-threshold J/ψ photoproduction signal, beyond that predicted solely by the quasi-free model, would therefore be an indication of the local "hot spot" scenario.

Chapter 3

Existing Data & Models Near Threshold

Prior to E03-008, existing J/ψ photoproduction data extended only from just above threshold; there was no published data below 8.2 GeV photon energy, and theoretical estimates showed variation over several orders of magnitude. The closest-to-threshold measurements come from Cornell and SLAC and provide data in the 9.3 to 21 GeV region. As with E03-008, these experiments detected coincident lepton pairs as evidence of J/ψ decay.

3.1 Data

The SLAC data [20] detected J/ψ particles via their decay to both e^+e^- and $\mu^+\mu^-$ pairs. A photon beam of between 13.5 and 21 GeV endpoint energy was produced via Bremsstrahlung off a 5% radiator. They measured production from both H_2 and D_2 targets, with the lepton pairs detected in magnetic spectrometers. Their random background was typically 1% for electron pairs

and 20-30% for muon pairs, and a background of Bethe-Heitler pairs was negligible. There is also unpublished single arm data [21] from this experiment, obtained from muon spectra after calculated background subtraction.

The data from Cornell [22] used a collimated photon beam with an energy of between 9.3 and 11.8 GeV, incident on a 2.9 g/cm^2 beryllium target. e^+e^- pairs were detected in coincidence in a pair of lead-glass calorimeters. The experiment had two sources of background, the Bethe-Heitler production of wide-angle electron pairs, and misidentification of photons as charged particles. With the assumption that the production from beryllium is 9 times greater than that from a nucleon, they obtained an elastic nucleon cross section of 0.7 nb at $E_\gamma = 11$ GeV which appears to be flattening out towards threshold. (It is worth noting that the Cornell data assumed a branching ratio of 7% for $J/\psi \rightarrow e^+e^-$, whereas the SLAC and current data assume a branching ratio of 6%.)

Sub-threshold charm photoproduction rates off various nuclei, including carbon, have also been calculated [23] assuming domination of the pQCD simple photon-gluon fusion process. Their calculation gives a total cross section of about 0.25 fb/nucleon for carbon with 5.5 GeV photons. However, their cross-section for photoproduction on a free nucleon at 11 GeV is about a factor of five below the Cornell value. Assuming the Cornell data is correct, one explanation for this is that the simple photon-gluon fusion mechanism may become overshadowed by multiple gluon exchanges in the threshold region[1].

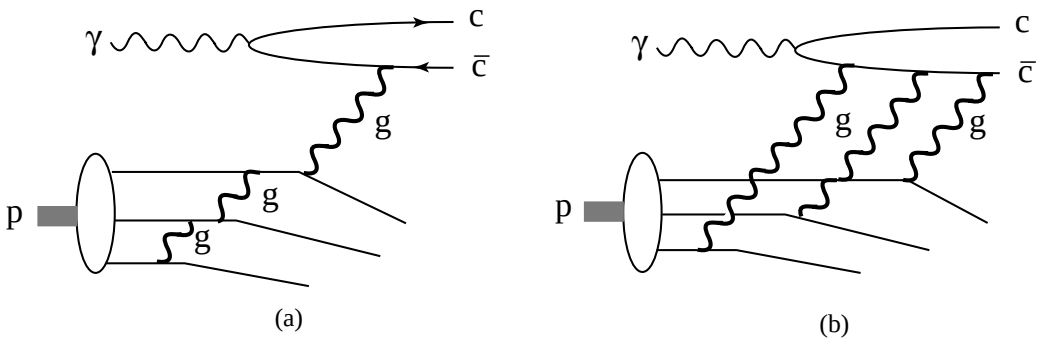

Figure 3.1: Two mechanisms for transferring most of the proton momentum to the charm quark pair in J/ψ photoproduction. The leading twist contribution (a) dominates at high energies, but higher twist contributions (b) become more important close to threshold.[1]

3.2 Theoretical Models

The experimental data is typically parameterised by the form $\frac{d\sigma}{dt} = Af(bt)$, with various forms of $f(bt)$ depending on different contributions. In the leading-twist contribution, most of the proton momentum is transferred to one valence quark which then interacts with the $c\overline{c}$ pair through the hard process $\gamma q \rightarrow c\overline{c}q$ (see Fig. 3.1a). Close to threshold however, this contribution ceases to dominate and higher-twist contributions from two- and three-gluon exchange become comparable (Fig. 3.1b)[3]. The higher-order contributions may even become dominant near threshold since i) there are many more diagrams of higher-twist processes, ii) they allow the proton to have a small transverse momentum component, and iii) the quantum numbers can match those of a particular charmonium state without extra gluon emission if several gluons couple to the quark pair.

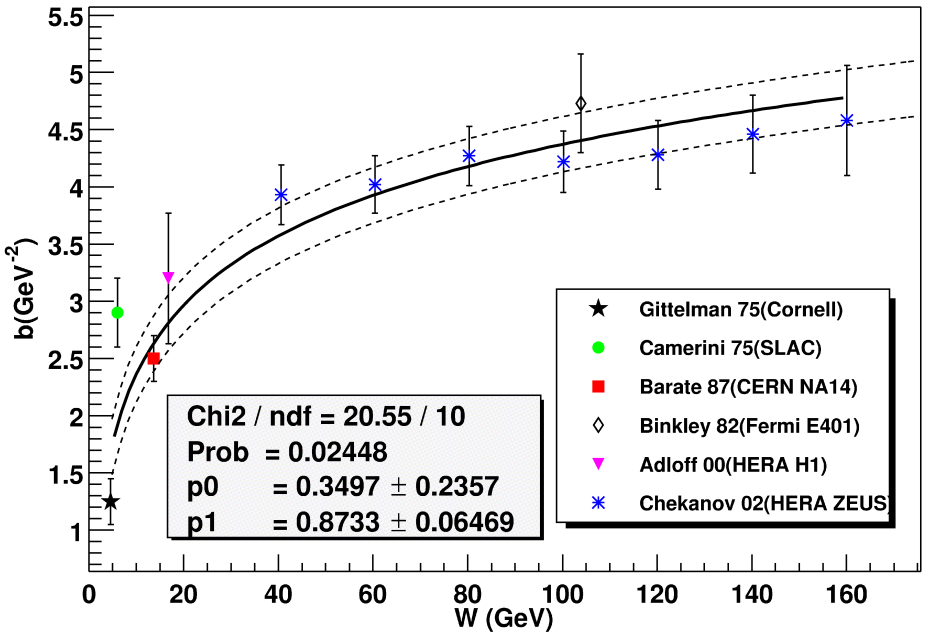

Figure 3.2: Slope parameter b from fits of the form Ae^{bt} to various J/ψ photoproduction experiments, as a function of $W = \sqrt{s}$.

The experiments from SLAC and Cornell use a cross section of the form $\frac{d\sigma}{dt} = Ae^{bt}$ for fits to their data. Values of b from a combination of these and other higher energy experiments are shown in Fig. 3.2; from the graph one would expect reasonable values of b in the sub-threshold region to range between 0 and 3. The value of b from Cornell is quoted as 1.25±0.2 GeV^{-2} at a photon energy of 11 GeV (though, as pointed out by [24], the actual slope of the data seems to be more like 1.5 GeV^{-2}). However, the SLAC value, at a 19 GeV photon energy, is given as 2.9±0.3 GeV^{-2}, more than twice that of Cornell. The difference between these two values makes it difficult to fit the data from both experiments with a smooth curve.

To take into account contributions from two- and three-gluon exchange, the fraction of the proton momentum carried by the valence (interacting) quark is given by

$$x = \frac{2mM_{J/\psi} + M_{J/\psi}^2}{s - m^2} \tag{3.1}$$

where $x \to 1$ at threshold. The momentum fraction carried by the spectator partons thus goes to zero as $x \to 1$. From QCD quark counting rules, the behaviour of the cross section near $x = 1$ is given by $(1-x)^{2n}$, where n is the number of spectator quarks in the interaction[25]. Thus the cross section for two gluon exchange - scattering on two quarks ($\gamma qq \to c\bar{c}qq$) - takes the form[1]:

$$\frac{d\sigma_{2g}}{dt} = N_{2g}\frac{(1-x)^2}{R^2M^2}F_{2g}^2(t)(s-m_p^2)^2 \tag{3.2}$$

while for three gluon exchange ($\gamma qqq \to c\bar{c}qqq$)

$$\frac{d\sigma_{3g}}{dt} = N_{3g}\frac{1}{R^4M^4}F_{3g}^2(t)(s-m_p^2)^2 \tag{3.3}$$

where the factor $\frac{1}{R^2M^2}$ is the relative weight of scattering from multiple quarks, with $R \approx \frac{1}{m_c} \approx 1fm$ and $M = 2m_c$ [26]. N_{2g} and N_{3g} are coefficients normalizing the curves to the experimental data from SLAC and Cornell. The $(s-m_p^2)^2$ term comes from the spin-1 nature of gluon exchange, and the coupling of the incoming photon to the $c\bar{c}$ pair [27]. The nucleon form factors $F_{2g}^2(t)$ and $F_{3g}^2(t)$ are not explicitly known, but parameterised as a function of b and t.

Fig. 3.3 shows the total cross sections from the Cornell and SLAC data as a function of incident photon energy. The curves are given by the above formulae with both proton form factors parameterised by $F^2(t) = e^{1.13t}$ according

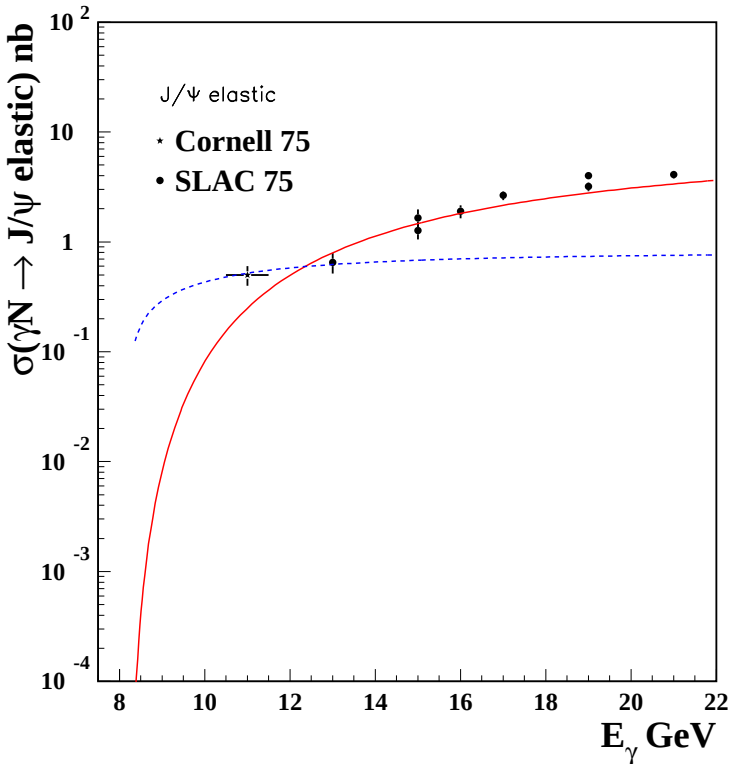

Figure 3.3: Total cross section for exclusive J/ψ photoproduction from a proton as a function of photon energy. The steeper (flatter) curve is the simple 2-gluon (3-gluon) model of [1], normalised to the data at 12 GeV.

to the experimental t dependency of the cross section [22]. While both curves drop off rapidly with photon energies approaching threshold, the combined data appears to be flattening out below 12 GeV; a possible explanation is a dominance of the 3-gluon process over the 2-gluon process near threshold, because the weaker s dependence of the 3-gluon process enhances the cross-section by a factor of $(1-x)^{-2}$[1]. However, as shown in [24], this flattening may still be explained by 2-gluon exchange, since in their formalism a different definition of x with a maximum value of about 0.8 is used, so the factor

$(1-x)^2$ is not so greatly suppressed.

Ref. [24] writes the t-dependence of the nucleon two-gluon form factor as a dipole form

$$F(t) = (1 - \frac{t}{m_{2g}^2})^{-2} \tag{3.4}$$

with $m_{2g}^2 \approx 1$ GeV^2 providing a reasonably good fit to all data up to $k = 100$ GeV (similar parameterizations work well for Pomeron coupling with the nucleon in the case of soft physics [28], though in that case the mass scale $\frac{1}{m^2}$ is close to the electromagnetic one). Using equation 3.5 for the dipole form factor squared, a reasonable fit to the low energy data was found to be given by

$$\frac{d\sigma}{dt} = \frac{2.5}{(1-t)^4} \text{ nb/GeV}^2 \tag{3.5}$$

corresponding to the 3 gluon exchange model of [1].

In short, there are many uncertainties in extending the current above-threshold cross section models to photon energies below 11 GeV. The various methods and models used in the context of the present experiment are discussed in chapter 6.

3.3 Quasi-free Modeling

For the simulations relating to this experiment, the following convolution integral was used to model the quasi-free photoproduction of a J/ψ from a heavy nucleus:

$$d\sigma = \int \Phi(k)dk \int \frac{d\sigma_0(s,t)}{dt} \alpha_{LC}(P_m, E_m) S(E_m, \vec{P}_m) d^3\vec{P}_m dE_m dt \tag{3.6}$$

similar to the model for the deuteron described in [1]. Here, s and momentum transfer t are functions of E_m, $\vec{P}_m$, and photon energy k, and the integral over $\vec{P}_m$ and E_m is limited to the kinematically allowed region described in section 2.2. $\Phi(k)$ is the photon flux, which is given by a/k, where a is the sum of half the target thickness in radiation lengths, and an effective quasi-real electroproduction factor [29] of 0.02. $d\sigma_0(s,t)/dt$ is the cross section for J/ψ photoproduction from a free nucleon, assuming that the neutron and proton cross sections are equal for simplicity. The carbon spectral function [30] $S(E_m, \vec{P}_m)$ is defined as the probability of finding a nucleon of momentum $\vec{P}_m$ and energy E_m in the nucleus. The flux term [31]

$$\alpha_{LC}(P_m, E_m) = (1 - \frac{E_m}{m} - \frac{\vec{k} \cdot \vec{P}_m}{km}) \tag{3.7}$$

averages to about 1.7 for the kinematics of this experiment.

Using this model for quasi-free production, the only unknowns in the equation are $d\sigma_0(s,t)/dt$, and the carbon spectral function at high $\vec{P}_m$ and E_m. Not taken into account in the present analysis is the fact that the elementary amplitude is far off shell (p^2 for the interacting nucleon is $\ll m^2$), which may lead to a suppression of the cross section.

Chapter 4

The Experiment

The Thomas Jefferson National Accelerator Facility (Jefferson Lab) is located in Virginia, USA. The accelerator site is separate from the user facility and requires special training and clearance for entrance. The site can be roughly divided into two sections, the accelerator facility, and the experimental halls; the accelerator produces the electron beamline and is controlled by the Machine Control Center (MCC), while the experimental halls are where the actual experiments take place, monitored by shift workers.

There are 3 experimental halls, A, B and C, that are supplied by the beam. Each hall is a different size and contains different types of detectors, allowing 3 different experiments to run simultaneously off the same beam. The MCC also controls the energy and current of the beam entering the halls, and can be set differently for each hall.

The beamline and halls are situated underground, the halls appearing from above as small round hills. A building nearby contains the Hall A, B and C

counting houses, which is where the specific experiments in their respective halls are controlled. During the running of an experiment three people are required to be on duty in the counting house at all times: a Shift Leader, a Target Operator and a Third Person, made up of physicists and students. The day is broken into three 8-hour shifts, and students are encouraged to be on shift duty each day of their respective experiments.

The data for this experiment was taken in November/December 2004 in Hall C. From previous above-threshold data the cross section was known to be extremely small, so a clear and unambiguous signal was needed with a very small background. The best way to measure this was to detect the e^-e^+ and $\mu^-\mu^+$ lepton pairs produced from J/ψ decay (6% branching ratio each). The pairs were detected in coincidence in the Hall C High Momentum and Short Orbit Spectrometers (HMS and SOS) and their originating particles' masses were reconstructed from measurements of the leptons' kinematics.

4.1 Beam & Target

The Continuous Electron Beam Accelerator Facility (CEBAF) is the heart of Jefferson Lab, and is responsible for producing a high intensity effectively continuous-wave electron beam, with a maximum energy of 6 GeV at 100 μA current, and greater than 75% polarization [32]. The continuous-wave nature of the beam is essential for reducing accidental coincidences to an acceptable level, especially in the context of the present experiment where rates are expected to be low. CEBAF comprises two antiparallel superconducting linear accelerators linked by nine recirculation beam lines for up to five passes.

The tunnel containing the accelerator magnets is built 7.62 m under the ground, and the magnets cooled by liquid helium from the refrigeration plant. After the final orbit the beam enters the switchyard and is delivered to one of the three experimental halls.

4.1.1 Beamline

The maximum energy of the beam at the time of data taking for this experiment was 5.76 GeV due to accelerator limitations, with a typical current of 60 μA and integrated beam charge on target of 27 C during the production runs. All components of the beamline from the extraction point at the switchyard to the target are controlled by the MCC. Because of the high intensity and small size of the beam, a raster is necessary to move the beam horizontally and vertically to prevent damage to the target material by overheating. This is achieved by the use of vertical and horizontal air-core magnets, also controlled through the MCC.

To normalise the counts obtained for the experiment, it is necessary to know the current of the incoming electron beam. There are four beam current monitors along the beamline, three RF cavities (BCM1, 2 and 3) and a paramagnetic current transformer (Unser monitor). The Unser, BCM1 and BCM2 are located behind the raster, while BCM3 is situated just before the target chamber. The RF cavities measure the relative beam current through the power of the RF radiation coupled in the cavity.

4.1.2 Target Chamber

The Hall C target chamber is an aluminium cylinder with an inner diameter of 1.232 m, and a 6.35 cm thick wall, situated at the pivot axis of the two Hall C spectrometers. There are openings in the left and right sides of the chamber to accommodate the full angular range and acceptance of the two spectrometers. The HMS opening is 20.32 cm tall and covered with a 0.04 cm thick aluminium window. The window for the SOS is 0.02 cm thick, covering an opening 12.7 cm tall.

The chamber is operated under vacuum, and the top plate of the cylinder has openings for the vacuum pumps, cryotarget plumbing, as well as a tube for the solid targets. There are also openings at the front and back of the chamber, where the beam entrance and exit tubes are attached.

4.1.3 E03-008 Targets

The J/ψ production data for the experiment were taken using a 2.5 g/cm^2 (in the beam direction) thick solid ^{12}C target, corresponding to a 6% radiation length. We had an effective real photon flux of 0.05 dk/k due to Bremsstrahlung of the electron beam on the target (3%, assuming half the real photons produced were usable), and from small-angle electroproduction (2%). A narrow target width of 5 mm was chosen to minimise the number of π^0 photons converting to electrons/positrons as they leave the target.

After the production runs, a series of runs were done for verification purposes. Liquid hydrogen was circulated through the cryotarget system for baryon

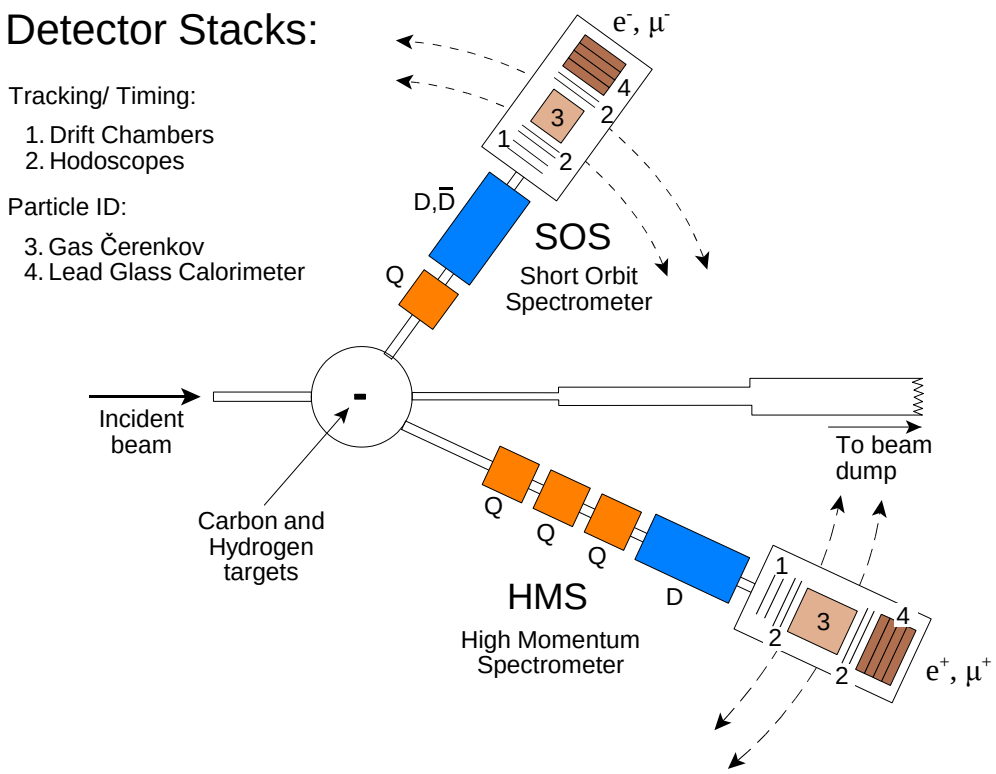

Figure 4.1: Diagram of the Hall C spectrometers and their component detector parts. The Q and D refers to quadrupole and dipole magnets respectively; the bar refers to a magnet of opposite polarity.

electroproduction at various spectrometer settings. A solid 3% beryllium target was also used, for ω and ϕ production. These runs are discussed in more detail in Chapter 5.4.

4.2 Hall C Spectrometer Setup

Hall C at Jefferson Lab houses two magnetic focusing spectrometers off the target chamber, designed to detect particles in coincidence. The High Momentum Spectrometer (HMS) was set to detect positively charged leptons e^+, μ^+ of central momentum 3.5 GeV and central scattering angle 24°, while the Short Orbit Spectrometer (SOS) detected the negatively charged leptons e^-, μ^- at a central momentum of 1.7 GeV and angle 53°. Both spectrometers are equipped with dipole and quadrupole magnets; the dipole magnets for momentum selection via deflection of charged particles, and the quadrupoles for focusing of the particles into the detector plane. In addition, both spectrometers can be moved around the experimental hall on rails, for different angular settings. The dipole magnets in both spectrometers are angled upwards towards the detector hut, so that the momentum and angle measurements are decoupled.

Both spectrometer arms are able to record the full kinematics of each detected particle, using a stack of different detector elements housed in a large concrete detector hut behind the magnets. A brief discussion of how each detector element works is included here, for a more detailed account see Refs [33, 34, 35].

At the front end of each detector hut are two wire drift chambers consisting of parallel gold-plated tungsten wires, spaced 1 cm apart and filled with a mixture of argon, ethane and isopropyl alcohol. In a drift chamber, particles traveling through the chamber ionise the gas, and the ionised electrons drift

to the wires thus producing a signal. Measuring the time between wire signals provides information on the location of the particle. By stacking a number of drift chambers with wires in different orientations together, accurate measurements of the particle's momentum and trajectory can be obtained. In the Hall C spectrometers, the resolution is better than 0.2%, and measurements of the scattering angle can be made with an accuracy of between 1 and 3 mrad, resulting in an overall resolution on the di-lepton mass of 10 MeV.

Behind the drift chambers are two pairs of scintillation paddles. The paddles are made out of PVT (polyvinyltoluene), a material that emits light when traversed by energetic particles; this light is detected and converted into an electronic signal by photomultiplier tubes attached to the ends of the paddles. The scintillators provide a trigger for the data acquisition system, as well as accurate time of flight measurements of the particles, used for background rejection and particle identification.

In between the two layers of scintillator paddles in each spectrometer is a gas Čerenkov counter, which works by detecting the number of Čerenkov photo electrons produced by a particle traveling through a gas chamber when the particle's velocity is greater than the speed of light in the gas ($\beta = v/c > 1/n$). Since the speed of light depends on n, the refractive index of the gas, the threshold for Čerenkov radiation being produced can be tuned by adjusting the gas type and pressure in the Čerenkov's tank, allowing for particle separation and identification. The Čerenkovs used in the HMS and SOS differ in their construction and overall efficiencies, and are discussed in

their relevant sections below.

Finally, a calorimeter measures the energy of a particle by the number of photons produced when the particle moves through a large block of material at the back of each spectrometer. For electrons and photons this is the total energy as the Hall C calorimeters correspond to 16 of their radiation lengths. For pions, however, there are not enough interaction lengths for the particles to stop in the calorimeter, hence only a fraction of their energy is measured.

In the case of the Hall C spectrometers the calorimeters are made of four layers of lead glass, so the photons are produced by the Čerenkov effect. The calorimeter provides particle identification through the amount of energy deposited in each layer by the particle, compared to the particle's total momentum.

The interior of the spectrometers are maintained under vacuum from the pivot at the target to the detector hut, to reduce multiple scattering within and prevent resolution degradation as much as possible. At either end are composite Mylar/Kevlar vacuum windows, thin enough to have a minimal effect on the beam, yet strong enough to withstand the pressure resulting from the vacuum. The radiation length of the Mylar used is 28.7 cm. The density of the Kevlar is 0.75 g/cm^3, with a tensile strength of 900 lbs/inch and a radiation length of 55.2 cm. The same composite material is used for the windows in both the HMS and SOS.

The HMS entrance window (target end) is round, with a 26.67 cm diameter. The exit window, located in the detector hut, is the largest window in the hall, with a bolt-hole diameter of 101.6 cm. This window withstands 74 425 N.m^{-2} of pressure, protecting the detector elements from the vacuum.

The SOS entrance window is also round, with a diameter of 22.86 cm, slightly smaller than the HMS entrance window. The exit window in the SOS, however, is rectangular, with dimensions of 102.87 by 16.51 cm. This is the second largest window in the hall, withstanding a load of 17 275 N under vacuum. A more in-depth discussion of the vacuum windows is described in [36].

The coordinate system for both spectrometers is as follows: z is along the beamline, down the central axis of each spectrometer. The x-axis points in the dispersive direction, with downwards being positive. The y-axis is then chosen to point left, to make the coordinate system right handed.

4.2.1 The High Momentum Spectrometer (HMS)

The HMS spectrometer is situated on the right side of Hall C when viewed from above, and is 26 m in length. The HMS is the key to Hall C's experimental capabilities, with its wide central momentum range of 0.5 GeV to the high value of 7.5 GeV from which it derives it's name.

The HMS carriage can be rotated along rails to a forward angle of 12.5°, and to a backwards angle of ∼90°. The angular values are marked on the floor,

and cameras are installed on the carriage to give a readout of the current angular setting to the counting house. The HMS can be rotated remotely from the counting house, using motors attached to the carriage. Table 4.1 summarises these specifications for the HMS.

At the front of the spectrometer, mounted to the front of the first quadrupole is a collimator made of 6.3 cm thick 90% W, 10% Cu/Ni alloy. The collimator is octagonal in shape, and used to restrict the background of the spectrometer; the collimator cuts out multiple scattering from other elements in the spectrometer, and while producing some small background of its own provides a single known source for background which is easier to cut out in the data analysis.

HMS Magnets

The HMS magnets consist of three superconducting quadrupoles, labeled Q_1, Q_2 and Q_3, followed by one superconducting dipole D. The magnets are cryogenically cooled by circulating liquid helium. The power supplies for the magnets are water cooled, and the total water flow needed for cooling all four magnets is about 80 litres per minute. The temperatures of the magnets are monitored at the rear of the spectrometer, and during runs are visible on the HMS control screen in the Hall C counting house.

The quadrupole magnets are used for the transverse focusing of the beam, and are made from iron. Q_1 is 2.34 m long with an effective length of 1.89 m, an inner pole radius of 25 cm, and weighs 20 tons. Q_2 and Q_3 are iden-

Table 4.1: HMS Specifications

Quantity	Specification
Momentum	
Maximum Central Momentum	7.5 GeV
Momentum Bite	18%
Momentum Resolution	0.1%
Acceptance	
Solid Angle	≈7 msr
Horizontal Acceptance	±27.5 mrad
Vertical Acceptance	±70 mrad
Useful Target Length	10 cm
Kinematic Flexibility	
Momentum Range	$0.5 \rightarrow 7.5$ GeV
Angular Range	$12.5^\circ \rightarrow 90^\circ$

tical, being 2.60 m in length (2.10 m effective length), and having an inner radius of 35 cm. Q_2 and Q_3 weigh 30 tons each. The dipole magnet is used for selection of the central momentum of the spectrometer, which is set remotely from the counting house. The magnet separates particles of different momenta in the dispersive (x) direction, bending particles of the correct momenta up towards the detector hut. The HMS dipole magnet measures 5.99 m in length, 2.95 m wide, and 4.46 m in height. It has an effective length of 5.26 m and a bending radius of 12.06 m, which results in a 25° bending angle at a central momentum on 4 GeV. The HMS dipole weighs in at a hefty 470 tons.

The Q_2 and D magnets are set with polarities the same sign as the charged particles set to be detected in the HMS detector hut (ie. positive for E03-008), and the Q_1 and Q_3 magnets are set to polarities of the opposite sign (ie. negative for E03-008).

HMS Detector Elements

Drift Chambers

There are six planes making up the HMS drift chambers, labeled as follows: X, Y, U, V, Y', X'. The X and X' wires measure particle position along the dispersive direction, the Y and Y' wires measure along the transverse direction, and the U and V wires are oriented at an angle of 15 degrees with respect to the X planes. The wires are of two thicknesses: the 30 μm wire is held at ground potential, and the thicker 60 μm wire holds a high negative potential.

Table 4.2: Scintillator Dimensions in the HMS and SOS

	Thickness (cm)	Width (cm)	Length (cm)	Number
HMS X1 & X2	1.0	8.0	75.5	32
HMS Y1 & Y2	1.0	8.0	120.5	20
SOS X1	1.0	7.5	36.5	9
SOS Y1	1.0	4.5	63.5	9
SOS X2	1.0	7.5	36.5	16
SOS Y2	1.0	4.5	112.5	9

The drift chambers are filled with a mixture of argon (49.5%), ethane (49.5%) and isopropyl alcohol (1% by weight). The gas bottles are kept behind the gas shed outside the counting house. The gas shed holds the gas mixer which electronically mixes the argon and ethane. The alcohol is added by bubbling the gas through a refrigerated bubbler. Both the argon and ethane bottles have regulators that read the gas pressure in the bottle and line. Gas log books must be completed during each shift, to monitor the amount of gas left in the bottles. The reading for the ethane however is by weight, since the ethane in the bottle is in liquid form, and the bottle sits on a scale for this purpose.

Scintillator Hodoscopes

Each pair of counters consists of two layers of scintillator paddles, S1X and S1Y at the front, and S2X and S2Y behind the Čerenkov. The "X" layers are oriented horizontally, for tracking along the x axis, with 32 scintillator

units in each, and the "Y" layers vertically, for tracking along the y axis, with 20 units per layer.

The dimensions of the scintillators paddles are shown in table 4.2. The maximum emission wavelength of the scintillators is 408 nm. Each scintillator paddle is attached to two photomultiplier tubes (PMT's) - one on each end. The HMS scintillators are covered with one layer of aluminium foil followed by one layer of Tedlar PVF Film for light tightness.

Gas Čerenkov

The HMS Čerenkov is a large cylindrical tank of length 152.4 cm, and an inner radius of 47.7 cm. The ends of the cylinder are 1 mm thick and made of strong aluminium alloy sheeting. Two mirrors inside the tank focus the light produced by Čerenkov radiation onto two 12.7 cm PMT's.

The tank was filled with Freon-12 gas for E03-008. For positron identification, the gas pressure in the Čerenkov was set so that the threshold momentum for pions and heavier particles to produce Čerenkov light was higher than the maximum accepted HMS momentum. Separating muons from pions was trickier because of their similar masses, therefore the gas pressure in the HMS Čerenkov was fine-tuned so that the pion momentum threshold was about 8% above the central HMS momentum - just below the maximum accepted momentum. The muon momentum threshold was therefore 17% below the central HMS momentum, and below the HMS minimum accepted momentum. Thus muons traversing the HMS Čerenkov produced on average 2 to 4

photoelectrons over the spectrometer acceptance, compared to around 10 for (fully relativistic) positrons. Using a threshold of 1 photoelectron for triggering, the muon identification efficiency was between 85 and 8% depending on momentum.

Lead Glass Calorimeter

Four layers of leaded glass make up the HMS's calorimeter, the last detector element in the hut. Each layer consists of 13 blocks, with each block measuring 10 x 10 x 70 cm. At least one PMT is attached to each block to measure the amount of light produced.

4.2.2 The Short Orbit Spectrometer (SOS)

The 7.4 m Short Orbit Spectrometer sits on the opposite side of the hall to the HMS. It too can be rotated along rails between forward and backward angles of 14.5° and 168.4° respectively. The rotation can be controlled remotely from the counting house, with cameras giving readings of the angular scale with 0.5° intervals. A limit switch prevents remote rotation of the SOS to angles forward of 20°; in cases where such angles are required the spectrometer must be rotated manually within the hall.

The SOS collimator is attached to the vacuum can at the front of the SOS quadrupole magnet, and made of the same W/Cu/Ni alloy as the HMS collimator. It is also 6.35 cm thick and octagonal in shape, with the same purpose of reducing the experimental background.

Table 4.3: SOS Specifications

Quantity	Specification
Momentum	
Maximum Central Momentum	1.8 GeV
Momentum Bite	40%
Momentum Resolution	0.1%
Acceptance	
Solid Angle	≈9 msr
Horizontal Acceptance	±60 mrad
Vertical Acceptance	±40 mrad
Useful Target Length	4.4 cm
Kinematic Flexibility	
Momentum Range	0.1 → 1.8 GeV
Angular Range	14.5° → 168.4°

The SOS specifications are given in Table 4.3. The SOS was designed for a large solid angle and momentum acceptance with a short path length, especially suitable for detecting particles with short lifetimes, such as pions and kaons.

SOS Magnets

The SOS magnet configuration is Q_S, D, $\overline{D}$, one quadrupole magnet followed by two dipoles with opposite polarity. These are standard resistive magnets, and they and their power supplies are cooled via the Hall C Low Conductivity

Water System. All three magnets are equipped with Hall probes to monitor their respective magnetic fields. The power supplies are able to switch their output polarities, so that detection of positively or negatively charged particles in the SOS is possible. For E03-008, the polarity was set to detect negatively charged particles.

The Q_S magnet focuses in the non-bend (y) plane and defocuses in the bend plane. The dipoles then focus in the bend plane; the first dipole, D, provides an upward bend of 33°, while the second, $\overline{D}$, bends the beam downward by 15°. This results in an overall upward bend to the beam of 18°.

SOS Detector Elements

The SOS detector hut is made of high density concrete, with walls 61 cm thick on all sides to shield the detectors from high energy particles scattered from the electron beam. The inside walls are lined with 5 cm thick lead-box panels. The rear inside wall and the floor of the hut are lines with 5 cm steel plates. The same discussions on how the HMS elements work applies here.

Drift Chambers

The SOS drift chambers also consist of six planes of sensing wires, with the same momentum resolution of 0.2%. The chambers contain the same gas mix as in the HMS: Argon and Ethane piped through an alcohol bubbler.

The SOS drift chamber planes, however, differ to those of the HMS. In the SOS detector, particles pass through planes in the order U, U', X, X', V,

V'. The X and X' planes are the same orientation as those in the HMS drift chamber. The SOS U, U' and V, V' planes however are oriented at 60° to the X, X' plane and to each other.

Scintillator Hodoscopes

The scintillators in the SOS are nearly identical to those in the HMS, the only difference being in their number and dimensions. Table 4.2 shows a comparison between the HMS and SOS scintillators. The SOS scintillators differ in size between the two Y layers. The increase in length for the Y2 takes into account the acceptance flare in the dispersive direction.

Gas Čerenkov

As with the HMS Čerenkov the same differential technique was used to separate muons from pions, by calibrating the gas type and pressure in the tank. The useful momentum acceptance of the SOS spectrometer was -10% to +15% around the central momentum (during production runs) of 1.78 GeV, corresponding to momenta over the range P = 1.60 GeV to 2.04 GeV. Setting the pion threshold at 2.00 GeV (so that pions essentially never fired the Čerenkov), the muon threshold was 1.50 GeV - or $\beta = 0.9976$ - producing between 2 to 8 photoelectrons for muons, adequate for detection in the experiment.

Using C_4F_{10} which has an index of refraction of around 1.0014, a gas pressure of about 1.74 atmospheres was needed to achieve this threshold. The standard SOS Čerenkov tank could not be pressurised, so a new device was

required. It was decided to use the 1.6 GeV Čerenkov tank in storage at SLAC which could be pumped to vacuum, rather than build a new tank for the SOS Čerenkov mirrors, or modify the existing tank to hold pressure. The SLAC Čerenkov tank's acceptance was well matched to that of the SOS, the only major change necessary was shortening the radiator length to 0.9 m so that the tank fitted in the SOS hut. A brief description of the SLAC Čerenkov counter is given in Section II D 2 of Ref. [37].

Lead Glass Calorimeter

The calorimeter in the SOS is similar to that of the HMS, comprised of four layers of leaded glass blocks at the rear of the detector hut. In the SOS calorimeter, there are 11 blocks per layer, measuring 10 x 10 x 70 cm each. The blocks are also placed slightly asymmetrically to account for the flare in the acceptance of the SOS; 5 of the 11 blocks per layer are placed below the central line, while the remaining 6 blocks are above. Once again, the calorimeter provides determination of particle ID through the amount of energy deposited in each layer by the particle compared to its total momentum.

4.2.3 Spectrometer settings

The aim of the experimental measurement was to detect J/ψ mesons via their decay to e^-e^+ and $\mu^-\mu^+$ pairs. The SOS was chosen to detect the negatively charged particles, and the HMS the positively charged particles. For all the J/ψ production runs the HMS central momentum was set at 3.5 GeV, and it's angle was set to 24°. The SOS was set to a central momentum of 1.7 GeV, and an angle of 53° for the production runs. The spectrometer

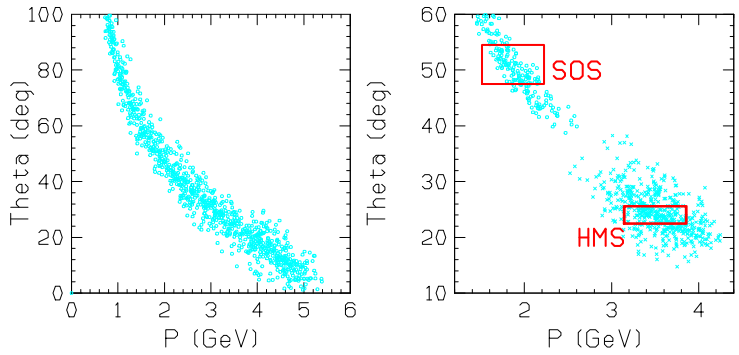

Figure 4.2: Momentum vs angle distribution of lepton pairs from J/ψ decay. (left) All generated pairs. (right) Lepton pairs detected in the HMS and SOS.

settings for all runs are shown in Table 4.4.

Through a Monte Carlo simulation the spectrometer settings were optimised according to the highest coincidence rates for forward angle J/ψ's. The simulation produced a sample of J/ψ's assuming a cross section model of the form

$$\frac{d\sigma}{dt} = \frac{2.5}{(1-t)^4} \text{ nb/GeV}^2 \tag{4.1}$$

as described in section 3.5 and the spectral function of Benhar[30]. The decay to lepton pairs was modeled to be asymmetric of the form $1 + \cos^2(\theta_{CM})$, assuming s-channel helicity conservation. Fig. 4.2 shows the distribution of all lepton pairs produced as well as pairs detected in the spectrometers. The square boxes show the acceptance coverage of the SOS and HMS at their momentum and angle settings for E03-008, chosen corresponding to the kinematics producing the highest rates.

Table 4.4: E03-008 Run Summary

Run Number	Target	Purpose	θ_{SOS} (°)	P_{SOS} (GeV)	θ_{HMS} (°)	P_{HMS} (GeV)
51917-52086	6% C	J/ψ production	53	1.69	24	3.5
52087-52089	-	Cosmic rays	-	-	-	-
52090-52099	LH2	Data checks	53	1.69	13	3.5
52100-52104	LH2	Data checks	40	1.69	13	3.5
52105-52124	LH2	Data checks	27	1.69	13	3.5
52128-52131	LH2	Data checks	27	1.69	13	2.5
52133-52138	LH2	Data checks	27	1.00	13	2.5
52148-52153	3% Be	$\omega \rightarrow e^- e^+$	25	0.9	11	1.95

4.3 Data Acquisition System

The trigger for the experiment was a coincidence between the pretriggers (or singles triggers) from each of the spectrometers. Both single arm pretriggers (HMS and SOS) were the requirement of a signal in three out of the four scintillator planes. These pretrigger signals are passed to the coincidence electronics, a programmable 8LM logic module that determines which kind of data acquisition (DAQ) trigger to produce. The module would not produce a DAQ trigger if the DAQ system was not ready to accept an event. The timing between the spectrometer pretriggers were adjusted to allow a coincidence window of 58 ns.

The valid signal is then passed to the trigger supervisor module, which controls the DAQ by sending gates to the ADC and TDC (analog-to-digital and time-to-digital conversion) modules, located in FastBus crates. The trigger supervisor also provides any prescaling necessary, though coincidence events were not prescaled. When the ADC/TDC module receives a gate, the hit information is stored in the module buffer memory until read out by the DAQ system.

The computers responsible for the data acquisition run CODA (CEBAF Online Data Acquisition) software, responsible for controlling the runs and the live analysis of the information obtained from the detectors for each event [38]. The CODA event builder collects the readouts from the detectors in the two spectrometers and combines the data into a single event which gets written to disk, and backed up later to magnetic tape. This is then converted

into a data ntuple which is used in the experimental data analysis.

4.4 Experimental Backgrounds

The main source of experimental backgrounds for e^-e^+ pairs is photoproduction of two mesons, one decaying with an e^- and the other with an e^+ in their final states, which trigger in coincidence in the spectrometers. Or, an electron scatters within the detector producing a meson which has an e^+ in its final state.

The second contribution to the e^-e^+ background is wide angle Bethe-Heitler pair production by high energy photons. Without good mass resolution this would have been the dominant background, such as in previous experiments [20, 22]. However, at the expected resolution of this experiment, from simulations of pair production using the formulae of [39, 40] and a monte carlo model of the detectors, the background of e^-e^+ Bethe-Heitler pairs was expected to be less than 10% of the J/ψ signal within 3σ of the J/ψ mass peak.

Finally, ρ, ω and η production may produce a very small background of e^-e^+ pairs, though the branching ratios of these is of the order of 10^{-5}.

The background for the $\mu^-\mu^+$ spectrum was expected to be somewhat larger than that for e^-e^+ pairs, since the Hall C spectrometers are less efficient at separating muons from pions, than they are for electrons (see section 5.2.3). Thus we expect backgrounds where pions are mis-identified as muons in the

detector. A second source is muons resulting from pion decays, with the correct kinematics to make it through the detector.

Chapter 5

Data Analysis

The analysis of the data was done using the ROOT Object-Oriented analysis framework [41] designed specifically for analysis of the large data sets attained in high energy physics experiments. This section describes the method of particle identification necessary in selecting the interesting events from the pool of data. It also covers the consistency and calibration checks done to ensure the detector elements and data acquisition systems were functioning correctly throughout the running of the experiment. Table 5.1 shows the variable names of some important quantities in the data ntuple used in the analysis.

5.1 Data Consistency Checks

5.1.1 Run List

The experimental data is taken in a series of runs to break up the large data sets that result into discrete, easier to manage files. Each run is typically

Table 5.1: Variables in the Data ntuple

Variable name	Description
cointime	Coincidence Time - the time between the detection of particles in the detectors, started by the SOS trigger and stopped by the HMS trigger
hsdelta	Deviation of the particle momentum from the HMS central momentum, $\frac{p-p_c}{p_c}$
ssdelta	Deviation of the particle momentum from the SOS central momentum, $\frac{p-p_c}{p_c}$
hsshtrk	Ratio of HMS calorimeter energy to particle momentum, E/p
ssshtrk	Ratio of SOS calorimeter energy to particle momentum, E/p
hcer_npe	Number of photo electrons produced in the HMS Čerenkov
scer_npe	Number of photo electrons produced in the SOS Čerenkov
ssxfp	x value in the SOS focal plane (cm) (positive x in the positive dispersion direction)
hpvec0	HMS particle energy
hpvecx	HMS particle momentum in the $x-$ (dispersion) direction
hpvecy	HMS particle momentum in the $y-$direction
hpvecz	HMS particle momentum in the $z-$ (beam) direction
spvec0,x,y,z	As for hpvec0,x,y,z
hshl1e	Energy deposited in HMS calorimeter layer 1
hshl2e	Energy deposited in HMS calorimeter layer 2
hshl3e	Energy deposited in HMS calorimeter layer 3
hshl4e	Energy deposited in HMS calorimeter layer 4
sshl1,2,3,4e	As for hshl1,2,3,4e

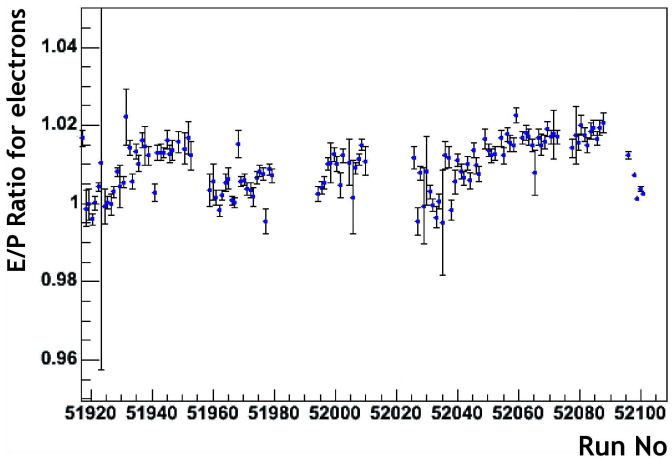

Figure 5.1: E/p peak positions for electrons per run

about an hour long; about 20 minutes into the run a series of online data checks are done by one of the shift workers in the counting house (usually the 3rd person), and if these checks show inconsistencies in the data the run is terminated, and a new run is started. These runs are discarded in the final analysis, as the data is unreliable.

A run also gets terminated if a magnet crashes or the high voltage power supply trips, the beam current drops, or any other component of the beamline or spectrometer encounters a problem. These runs are not discarded entirely, as most of the data is still good. Rather, the run is replayed through the event builder, stopping just before the end, so the good data can still be used in the analysis.

5.1.2 Energy vs Momentum Ratio in the Calorimeter

One of the quantities measured and saved in the data ntuple is the ratio of the summed energy deposited in the four layers of the calorimeter, to the particle's momentum. This is important for particle identification as an electron (positron) has low mass, so the energy it deposits into the calorimeter is roughly equal to its momentum at these extreme relativistic energies. That is, $E_e/p_e \approx 1$, where E_e is the energy deposited by the electron (positron) into the calorimeter. A pion is heavier, however, giving $E_\pi/p_\pi \approx 0.25$ (again, E_π is the energy deposited by the pion into the calorimeter). To ensure that the calorimeter was functioning correctly it is necessary to check that the data for electrons and pions reflect this property.

Fig. 5.1 shows the peak positions of detected electrons in the SOS calorimeter against run number, for the runs described in the section above. The data was obtained by extracting those events in each run in which an electron was detected, filling a histogram with the corresponding E_e/p_e value, and fitting a gaussian to find the mean. The figure shows the peak positions centered round 1 ($\pm 2\%$), showing that the calorimeter was indeed working correctly to detect electrons. The error bars in Fig. 5.1 are the statistical error resulting from the fit; those points with extremely large error bars are because of minimal data in that run.

Another important calorimeter check is to determine whether the E_e/p_e peak value is dependent on the position of the particle detected in the calorimeter. As shown in Fig. 5.2, the density of all particles incident on the calorimeter

is symmetric about the y-axis but not about the x-axis. Fig. 5.3 shows the E_e/p_e peak positions for all runs against their position on the x-axis of the calorimeter (the fits for each x-slice of this plot are shown in Appendix A). The error bars on this plot come from the error in the mean positions determined by the fit; for most points the error bars are too small to be seen. The last point's error bars are large due to the low statistics in that bin. There is a slight dependence on x position, as can be seen. However, since the deviation from 1 is at most 5% either way it was agreed that this effect could be ignored.

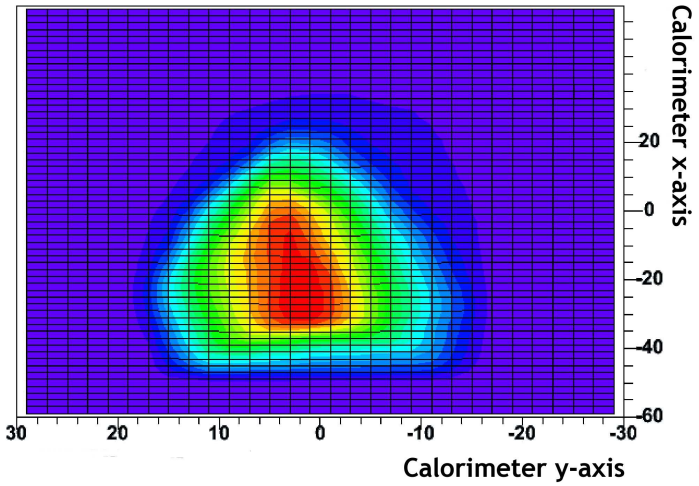

Figure 5.2: Electron density on the SOS calorimeter.

5.1.3 Čerenkov

The Čerenkov counters in the HMS and SOS were used to separate lepton pairs from pions in the detectors. While pions do not produce photo electrons from Čerenkov radiation, for the detector settings discussed above electrons

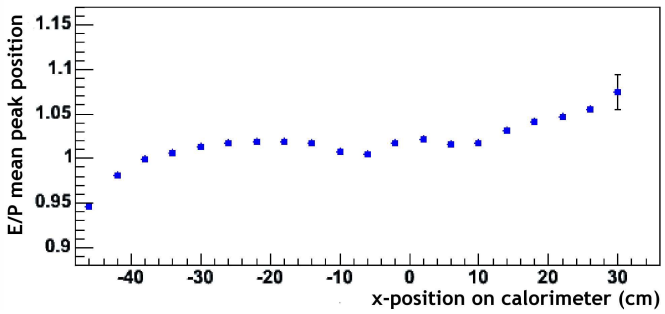

Figure 5.3: E/p peak values versus x-position on the SOS calorimeter.

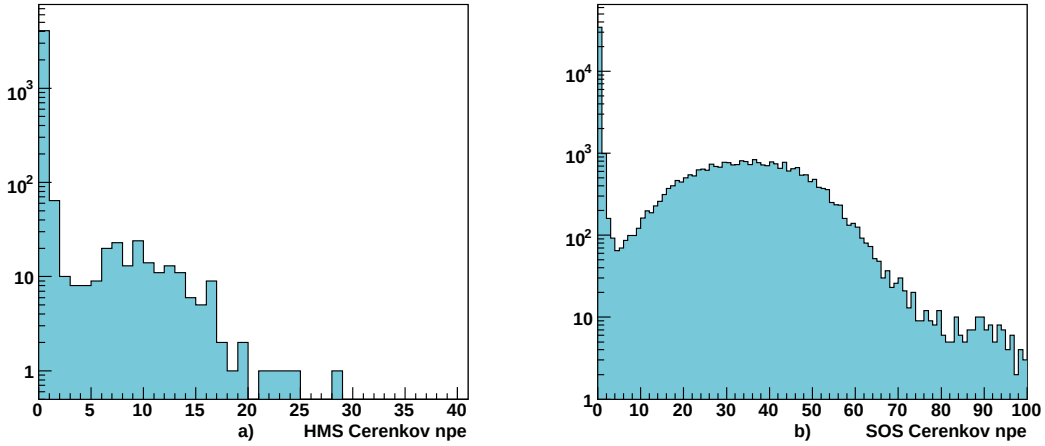

Figure 5.4: Number of photo-electrons (npe) produced in the HMS (a) and SOS (b) Čerenkov counters.

do. Fig. 5.4 shows the number of photo electrons produced from positrons and electrons in the HMS and SOS respectively. The large peaks in the zero photo electron bin of the histograms are from the electronic noise of the detectors.

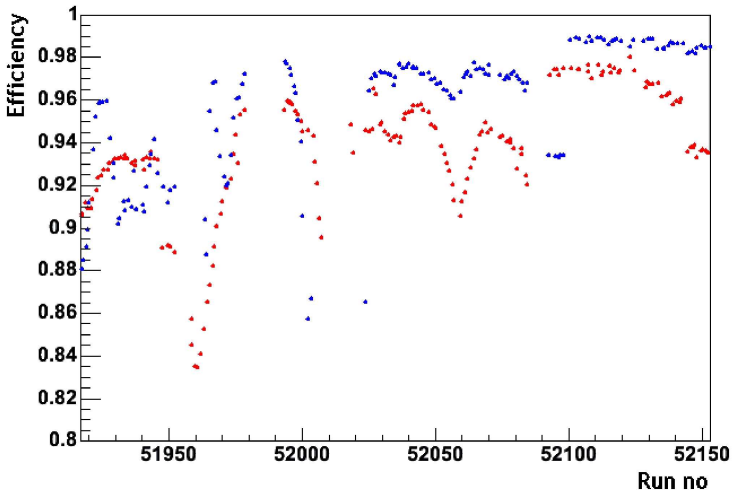

Figure 5.5: Tracking efficiencies in the HMS (red) and SOS (blue) for each run.

5.1.4 Tracking Efficiencies

The tracking efficiency per run is calculated by selecting events during the run with good scintillator triggers and good electron/positron identification (according to values preset in the online analysis code). The tracking efficiency is then defined as the number of good events with a particle track calculated, divided by the total number of good events determined from the experimental triggers. It is important that the efficiency be greater than 90% to ensure one is not losing valuable events. Fig. 5.5 shows the HMS (red) and SOS (blue) tracking efficiencies for all good runs in the experiment. For most of those runs the efficiencies were greater than 90%; those runs with efficiencies lower than 90% are a result of low beam current, or a magnet tripping near the end of the run.

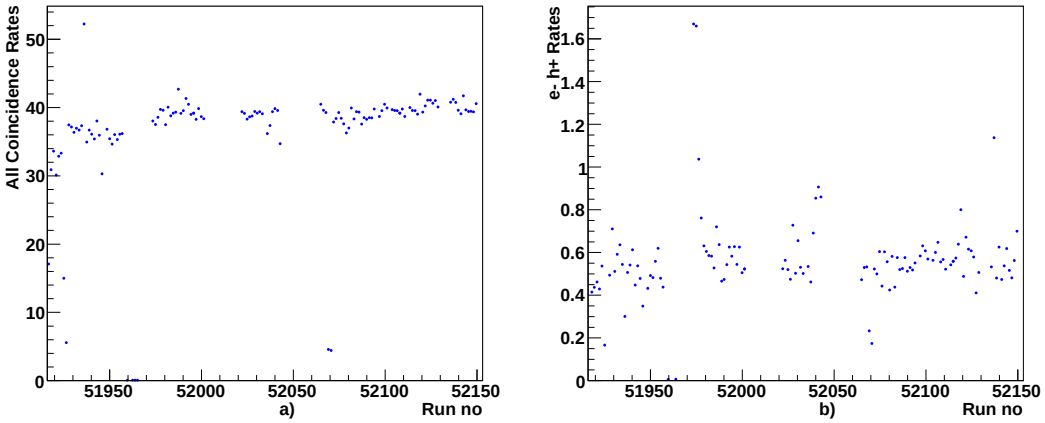

Figure 5.6: Coincidence rates for (a) all coincidences, and (b) electron-hadron coincidences.

5.1.5 Coincidence Rates

The total number of coincidences for each run was determined by counting the number of events in the coincidence ntuple that satisfied the cut on coincidence time (see section 5.2.4). This number was corrected for dead times and efficiencies of the detectors, and the coincidence rate was then found by dividing by the average beam current for the run. It is important that the coincidence rates are constant over the running of the experiment. The rates for all coincidences, and e^-, h^+ coincidences are shown in Fig. 5.6.

5.2 Particle Identification and Event Selection

The most important part of data analysis is in extracting the relevant events from the background of particles detected. Each different detector element adds its own information about the detected particle, and accurate identi-

fication of the particle can be achieved when all these are used together in the analysis. The interesting events are extracted by filtering through the entire ntuple with a specified set of cuts on the different variables shown in Table 5.1.

5.2.1 e^-, h^+ Identification

Since separating electrons from hadrons are the Hall C spectrometers' designed duties, the detectors have excellent capabilities for identification of these particles. To identify electrons from negatively charged pions in the SOS, the following cuts are required on the data:

1. The particle's momentum deviation from the central momentum was within the standard range: 15% below and 25% above ($-15 < ssdelta < 25$). This range is constant for all experiments, based on the known acceptance of the SOS.

2. The number of photoelectrons produced in the SOS Čerenkov counter was required to be greater than 2. ($scer\_npe > 2$)

3. The particle was required to deposit at least 70% of its momentum in the SOS lead-glass calorimeter. ($ssshtrk > 0.7$)

4. The x position of the particle at the SOS focal plane was required to be greater than -20. ($ssxfp > -20$) This is another standard cut for all SOS experiments, derived from the acceptance function of the spectrometer.

In the HMS, a further cut is made for positive hadron (such as π^+, p^+ or K^+) identification. The particles' momenta were required to be within 10%

of the HMS central momentum (|hsdelta| < 10). Again, this is a standard cut for all experiments and is based on the HMS acceptance function.

5.2.2 e^-, e^+ Identification

For separation of positrons in the HMS from the background of positive pions, two more cuts were made *in addition* to the above e^-, h^+ cuts:

1. The number of photoelectrons produced in the HMS Čerenkov counter was required to be greater than 3. ($hcer\_npe > 3$)

2. The particle was required to deposit at least 90% of it's momentum in the lead-glass calorimeter. ($hsshtrk > 0.9$)

These effectively extract the detected positrons for use in the reconstruction of the J/ψ, reducing contamination in the spectrometers while still keeping the efficiency of e^-, e^+ pairs to greater than 90%.

5.2.3 μ^-, μ^+ Identification

Hall C at JLab is especially good at separating positrons and electrons from the background of pions, however the spectrometers are not optimised for muon identification. While, at the energies of this experiment, electrons shower well in the various detector elements, muons and pions have relatively similar masses and both lose energy from ionisation, so the calorimeters cannot accurately distinguish between them. Differentiation of muons from pions was therefore done mainly with the Čerenkov detectors in the spectrometers (see section 4.2). Additionally, a number of cuts were made on the calorimeter variables, separating muons from the lighter electrons and

positrons by setting a maximum on the amount of energy deposited in each of the four calorimeter layers. Together the cuts produced an overall muon pair efficiency of 80%, and were:

1. The number of photoelectrons produced in the HMS Čerenkov counter was required to be greater than 1. ($hcer\_npe > 1$)

2. The number of photoelectrons produced in the SOS Čerenkov counter was required to be greater than 2. ($scer\_npe > 2$)

3. The particle was required to deposit only between 4 and 12% of its momentum in the first three calorimeter layers in both the HMS and SOS. ($0.04 < hshl1e(2e, 3e) < 0.12$ and $0.04 < sshl1e(2e, 3e) < 0.12$)

4. The particle was required to deposit only between 4 and 15% of its momentum in the final calorimeter layer, in both the HMS and SOS. ($0.04 < hshl4e < 0.15$ and $0.04 < sshl4e < 0.15$)

5.2.4 Coincidence Time

Finally, to ensure that the particles detected in the HMS and SOS originate from the same event in the target, a cut on coincidence time is made. Because of the differences in length between the HMS and SOS, the particles do not arrive in the spectrometers' detectors at the same time. The coincidence time is defined by the difference in the trigger time of the two spectrometers, $t_{SOS} - t_{HMS}$, and is measured in nanoseconds. The actual value of this quantity depends on the specifics of the experiment: the time difference expected for di-lepton pairs in the Hall C spectrometers is 58 ns (the difference between e^-, e^+, and μ^-, μ^+ pairs is negligible). A more useful quantity is

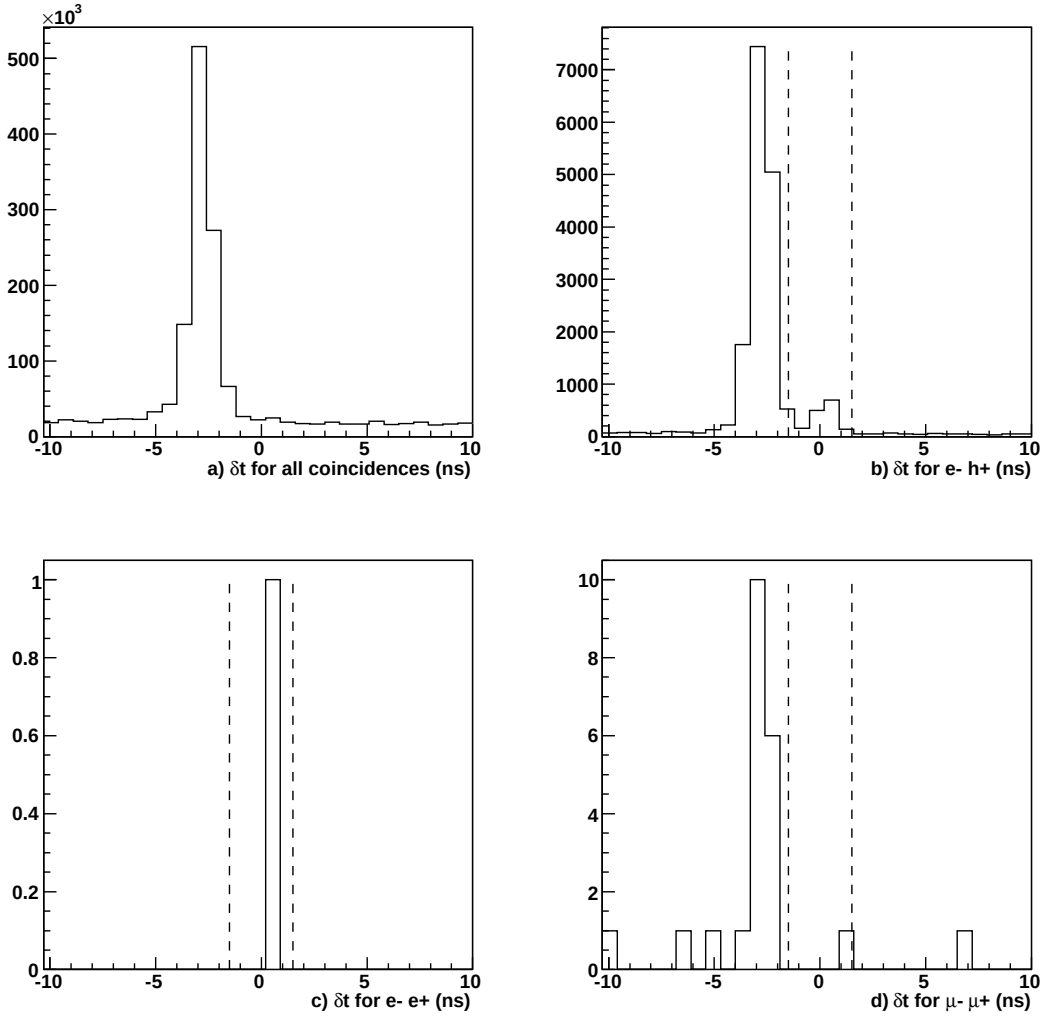

Figure 5.7: Coincidence spectra for the J/ψ production runs (ns). a) All coincidences, b) e^-, h^+ coincidences, c) e^-, e^+ coincidences, and d) μ^-, μ^+ coincidences.

δt, the actual di-lepton coincidence time relative to the expected di-lepton coincidence time. In the analysis of the data, events were rejected if their coincidence time differed by more than 1.5 ns to the expected ($|\delta t| < 1.5$ ns, shown as the vertical dashed lines in Fig. 5.7 below).

Fig. 5.7 shows the coincidence time histograms for the J/ψ production runs of the experiment. Fig. 5.7a shows the coincidence time spectra for all detected particles (ie no particle identification cuts); Figs. 5.7b, c and d show the coincidence time spectra for e^-, h^+, e^-, e^+, and μ^-, μ^+ coincidences respectively. The background events on the plots are the accidental coincidences, the coincident detection of particles that did not originate from the same event but are most often from multiple scattering inside the spectrometer. The histogram in Fig. 5.7b has two peaks, the peak at -3 ns is from e^-, p^+ coincidences, while the smaller peak near zero is from e^-, π^+ coincidences. Since pions and protons have different masses, there is a difference in the times of flight of these two particles, thus producing the two peaks.

We see only a single e^-, e^+ coincidence in Fig. 5.7c within the cut region, and there are no coincidences in the e^-, h^+ or accidentals region. Since the branching ratios for e^-, e^+ and μ^-, μ^+ decays are equal we would expect the same number of coincidences in the μ^-, μ^+ coincidence time spectrum. However, since the detectors are not as tuned for muon identification as they are for electron/positron identification most of the coincidences in Fig. 5.7d are probably muons coming from pion decays, or pions misidentified as muons.

5.3 J/ψ Reconstruction

Once the cuts described in section 5.2 were used to select coincident leptons from the background, the invariant mass $M_{l^-l^+}$ of the lepton pair was calculated using the following formulae:

$$\begin{aligned} E_{l^-} &= \sqrt{[m_{l^-}^2 + P_{l^-}^2]} \\ E_{l^+} &= \sqrt{[m_{l^+}^2 + P_{l^+}^2]} \\ M_{l^-l^+} &= \sqrt{[(E_{l^-} + E_{l^+})^2 - (\overrightarrow{P}_{l^-} \cdot \overrightarrow{P}_{l^+})^2]} \end{aligned} \tag{5.1}$$

where m_{l^-} and m_{l^+} are the masses of the leptons detected in the SOS and HMS respectively, and $\overrightarrow{P}_{l^-}$, $\overrightarrow{P}_{l^+}$ are their 3-momenta. The invariant mass spectra from the J/ψ production runs are shown in Fig. 5.8. Fig. 5.8a shows the mass spectrum for all detected events, Fig. 5.8b for $e^-, \pi+$ coincidences, and Figs. 5.8c and d for the di-lepton coincidences.

Figs. 5.8a and b show a smooth, continuous spectrum over the range 2.5 $< M_{l^-l^+} <$ 3.5 GeV, showing good phase space coverage of the spectrometers and good acceptance at the J/ψ mass of 3.097 GeV. There is only a single count in 5.8c, the e^-, e^+ mass spectrum, however. While this is a true coincidence (as seen from the corresponding coincidence time graph Fig. 5.7c), the mass of the event is 2.71 $\pm$ 0.01 GeV, more than 40 σ from the J/ψ mass. As such, this event is background, either an electron-pion event (with the pion mis-identified as a positron) or a wide-angle pair conversion of a Bremsstrahlung photon.

The μ^-, μ^+ mass spectrum shown in Figs. 5.8d has too only a single event,

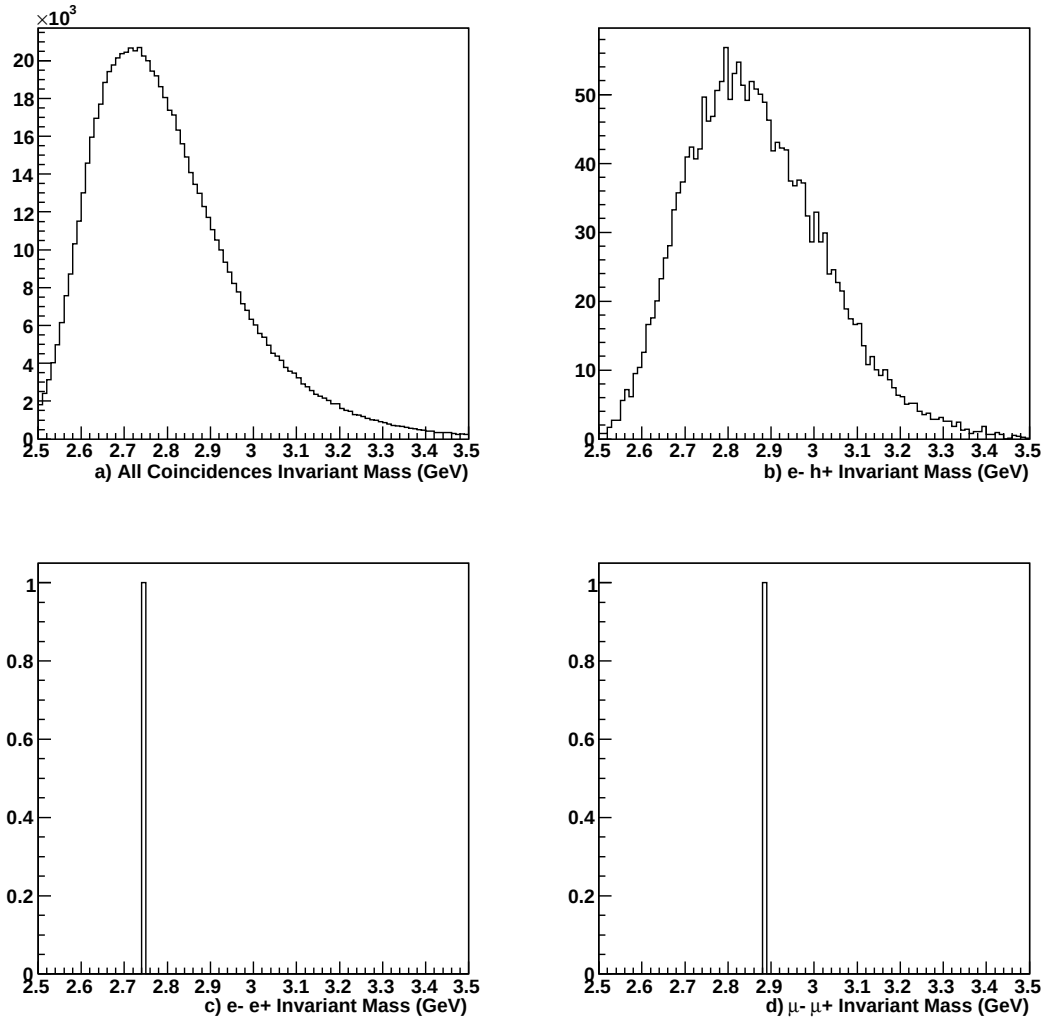

Figure 5.8: Reconstructed mass spectra for the J/ψ production runs. a) All coincidences, b) e^-, h^+ coincidences, c) e^-, e^+ coincidences, and d) μ^-, μ^+ coincidences.

at an invariant mass of 2.87 ± 0.01 GeV, more than 30 σ away. Once again, this event is background; most likely an accidental coincidence, but possibly another pair conversion, particle misidentification, or the decay of a pion to a muon pair.

The absence of a peak at the J/ψ mass has some important implications for the data analysis, namely in that an actual value for the sub-threshold J/ψ cross section cannot be obtained. This null result is no less important, however: we are able to investigate different models for the free nucleon cross section, and various methods of extrapolating the carbon spectral function to high values of missing momentum and energy, and compare their predictions to the observation of this experiment. It will be seen that the results are consistent with predictions of the quasi-free production mechanism, and therefore place limits on exotic mechanisms that may strongly enhance the sub-threshold cross sections.

5.4 Calibration Runs

After the J/ψ photoproduction runs, the target and spectrometer settings were changed, as shown in Table 4.4, to check the spectrometer settings and resolutions and make sure we see the expected peaks from known interactions. A liquid Hydrogen (LH2) target was first used for the production of nucleon resonances from electron-proton scattering. After the LH2 runs the target was changed to beryllium, to detect leptons resulting from ω decay.

5.4.1 Hydrogen Target Runs

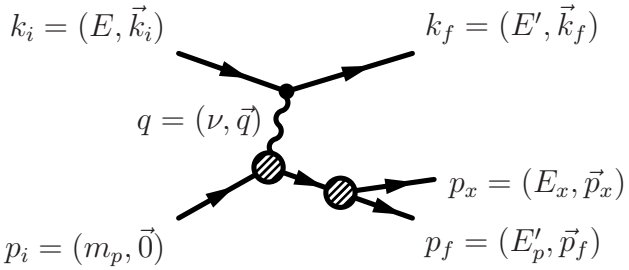

Figure 5.9: The one-photon exchange diagram of the resonance electroproduction process, where, for example, k_i is the four-momentum vector of the incoming electron composed of energy E and momentum $\vec{k}_i$.

For the first set of calibration runs the target was switched to LH2 circulated in a loop in the target chamber. The aim of these runs was to identify nucleon resonances via deep inelastic scattering of an electron off a proton. The Feynman diagram for this process is shown in Fig. 5.4.1, and the variables used to define the kinematic quantities used in the analysis are summarised in table 5.2. k is used to denote the four-momentum of the electron, p for the four-momentum of the proton, and q for the four-momentum of the virtual photon. The reaction is kinematically complete: the four-momenta of the incident electron and target proton are known, and both the scattered electron and proton's positions and four-momenta are detected, the electron in the SOS, and the proton in the HMS. The resonant state is labeled by mass W, and X describes any particle(s) resulting from the decay of this state that is (are) not detected in either the HMS or SOS. For an extensive analysis of these resonant processes, see Ref. [42, 43, 44].

The analysis of the hydrogen target runs is done by reconstructing the mass

Table 5.2: Variable Quantities in Hydrogen Target Analysis

Variable	Lab Frame Value	Description
k_i	$(E, \vec{k}_i)$	four-momentum of the incident electron
k_f	$(E', \vec{k}_f)$	four-momentum of the scattered electron
p_i	$(m_p, 0)$	four-momentum of the target proton
p_f	$(E'_p, \vec{p}_i)$	four-momentum of the scattered proton
q	$(\nu, \vec{p}_f)$	four-momentum transferred to the target

of, and thus identifying, the missing particles; these correspond to particular resonances of the nucleon which are well known. Since the full kinematics of the incident and scattered protons and electrons are known, the energy of the missing particle(s) can be calculated as $E_X = E - E' + m_p - E'_p$ where E and E' are the initial and final electron energies, m_p is the mass of the proton, and E'_p is the final proton energy. The missing momentum is given by $P_X = k_i - k_f - p_f$. Thus the mass squared of the missing particle(s) can be found by

$$M_X^2 = E_X^2 - |P_X|^2 \tag{5.2}$$

Kinematic Settings

The runs on the LH2 target that were used in the analysis were taken at three different kinematic settings, summarised in Table 5.3. The first kinematic setting has all but the HMS spectrometer angle set to the same values as used during the J/ψ production runs, with just the SOS spectrometer angle changing for the other two settings.

Table 5.3: Run Settings for LH2 Target

Run Number	Beam Energy (GeV)	P_{HMS} (GeV)	θ_{HMS} (°)	P_{SOS} (GeV)	θ_{SOS} (°)	Q^2	W (GeV)
52093 - 52098	5.77	3.5	13	1.69	53	7.76	0.88
52101 - 52104	5.77	3.5	13	1.69	40	4.56	2.0
52107 - 52124	5.77	3.5	13	1.69	28	2.26	2.5

The approximate four momentum transferred from the incident electron to the proton for each setting can be calculated using the SOS detector settings using

$$Q^2 \equiv -q^2 = 2EE'(1 - \cos\,\theta_e) \tag{5.3}$$

since E can be taken as the electron beam energy, and θ_e as the SOS angular setting. Furthermore, the invariant mass of the resonant state can be found using this calculated Q^2 by

$$W \equiv \sqrt{(q+p)^2} = \sqrt{m_p^2 + 2m_p\nu - Q^2} \tag{5.4}$$

With all three settings, the data cover a range of Q^2 and W values, resulting in 5 different observed missing mass peaks, giving greater confidence that the spectrometers and analysis programs were working correctly.

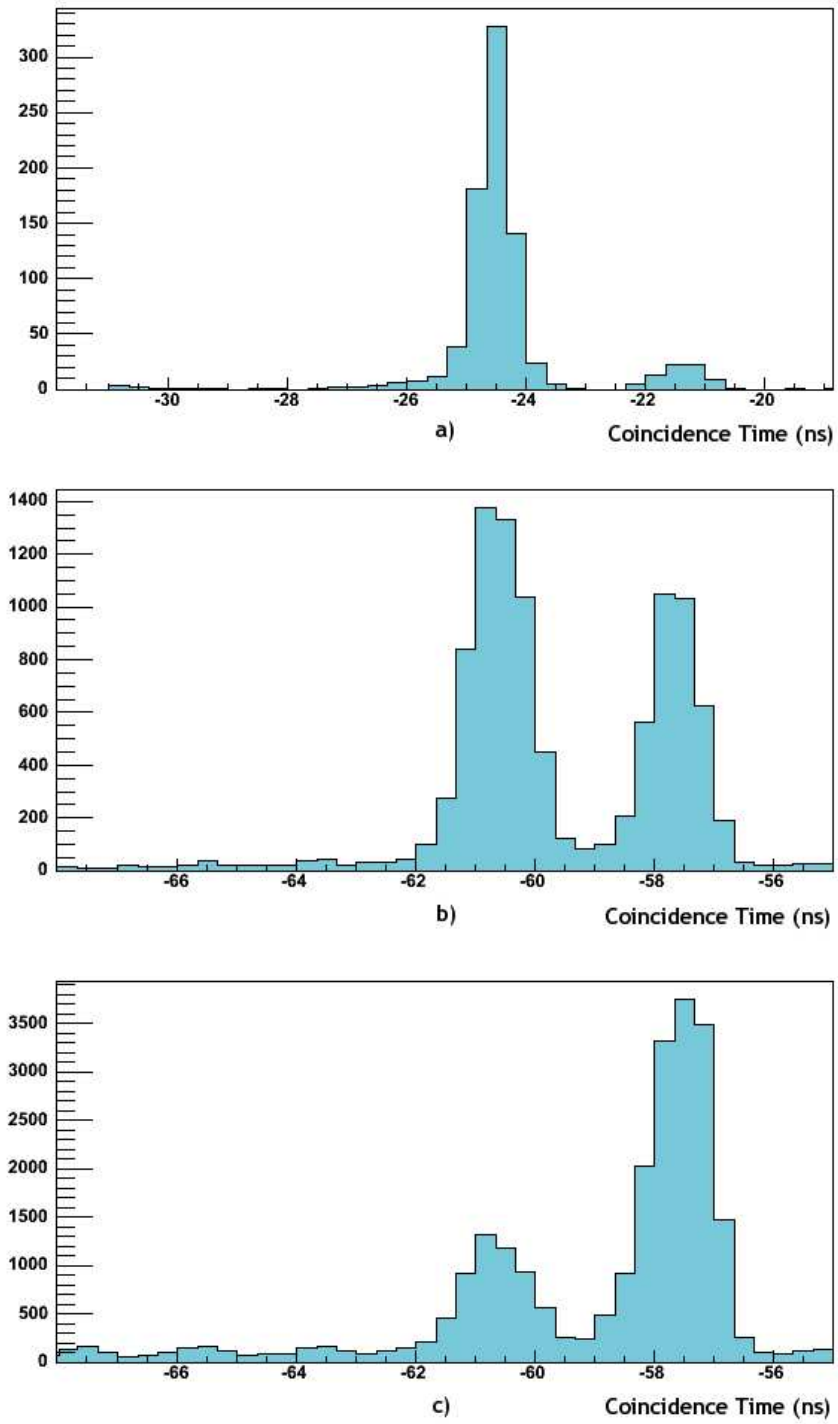

Figure 5.10: Coincidence spectra for the hydrogen target runs (ns), with a) θ_{SOS}=53°, b) θ_{SOS}=40°, c) θ_{SOS}=28°. The peaks on the left are from e^-, p^+ coincidences, while the peaks on the right are from e^-, π^+ or e^-, K^+ coincidences.

Coincidence Time Windows

The coincidence time windows for the LH2 runs differ from those of the J/ψ and omega production runs since different particles are being detected which have different times of flight; Fig. 5.10 shows the coincidence time spectra for each of the different kinematic settings. Three different coincidences are possible, between electron and proton, pion, or kaon, since a positive pion or kaon resulting from the decay of the nucleon resonance can also be detected in the HMS.

Only two coincidence time peaks are visible separated by about 2.5 ns, due to the differences in time of flight for the positive hadrons in the HMS (2.5 ns is the expected time of flight difference for protons and pions at pHMS = 3.5 GeV). e^-, p^+ coincidences form one clear peak(left), while e^-, π^+ or e^-, K^+ coincidences lie on top of each other in the coincidence time spectrum (right). The time of flight was normalised for a straight cut on pions in the online analysis code, this is the reason for the proton peak dependance on HMS momentum. The slight dependance of the second peak on HMS momentum is a result of the kaon coincidences in the peak.

Particle Identification Cuts

The standard cuts for electrons in the SOS, as described in section 5.2.1, were applied to select electrons from the background of negative pions. For particle identification in the HMS, a different set of cuts on the were used to select positive hadrons from the detected events:

1. The particle's momentum was required to be within 10% on either side of the HMS central momentum for the event to be physical. ($-10 < hsdelta < 10$)

2. The number of photoelectrons produced in the HMS Čerenkov counter was required to be less than 1, since hadrons do not fire the Čerenkov. ($hcer\_npe < 1$)

3. A large portion of a hadron's momentum in contained in its mass, so it was required that the particle deposits less than 70% of it's total momentum in the lead-glass calorimeter. ($hsshtrk < 0.7$)

Note that these cuts do not identify the different types of hadron from each other; the events recorded during the runs could be from electron-proton, electron-pion, or electron-kaon coincidences. The importance of this shall be seen in the missing mass analysis as the peaks from the resonance decays shift depending on which final particle mass is used in the calculation of M_X^2. In addition to the above cuts, cuts on the different coincidence time peaks were made, thus selecting protons, or pions and kaons. Since this was not the main analysis of the experiment we were not concerned with making a momentum-dependant cut along the proton peak; straight cuts, in addition to the particle identification cuts, were sufficient to exclude enough accidental coincidences for the analysis.

Missing Mass Peak fits

The missing mass squared (M_X^2) for each event of each run was calculated using equation 5.2. The large peaks visible above the multipion background

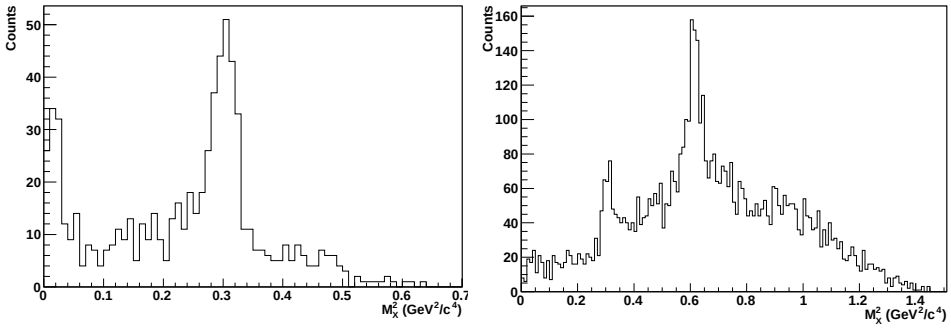

Figure 5.11: M_X^2 (GeV) calculated using proton mass, with a) θ_{SOS}=53°, b) θ_{SOS}=40°.

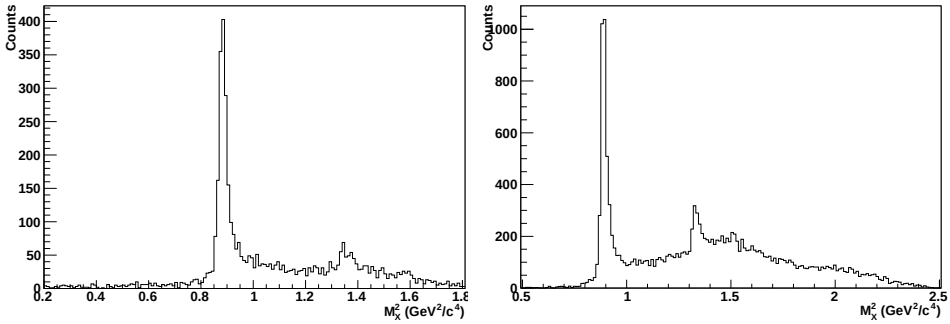

Figure 5.12: M_X^2 (GeV) calculated using pion mass, with a) θ_{SOS}=40°, b) θ_{SOS}=28°.

correspond to undetected particles from the decay of a resonance. The positions of each peak are obtained through a gaussian fit to the data; these fits can be seen in the figures in Appendix B. Fig 5.11 shows the M_X^2 spectra for the $\theta_{SOS} = 53°$ and 40° data assuming the hadron detected in the HMS has the mass of a proton, and cutting on the proton coincidence time peak. A clear peak at the η mass squared value of 0.3 GeV^2 is visible for both θ_{SOS} settings. Also, at $\theta_{SOS} = 40°$, the ω peak near 0.616 GeV^2 is clear. The results of the fits to these peaks are shown in Table 5.4.

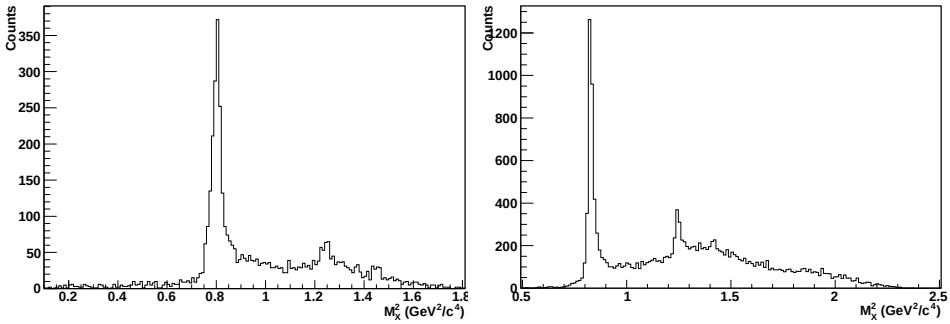

Figure 5.13: M_X^2 (GeV) calculated using kaon mass, with a) θ_{SOS}=40°, b) θ_{SOS}=28°.

If we place our coincidence time cut round the pion/kaon peak instead, we obtain the M_X^2 spectra for detection of these particles in the HMS. Using the π^+ mass in the calculation of M_X^2, the spectra are shown for $\theta_{SOS} = 40°$ and 28° in Fig. 5.12. At both θ_{SOS} settings a large peak near 0.9 GeV^2 is seen; this peak corresponds to an undetected neutron. A smaller peak round 1.3 GeV^2 is also visible at both θ_{SOS} settings; this is the peak from the Λ particle, shifted up from the Λ mass squared of 1.243 GeV^2 as a result of using the π^+ mass to calculate M_X^2.

Using, instead, the kaon mass in the calculation of M_X^2, with a cut on the pion coincidence time peak, the spectra for the $\theta_{SOS} = 40°$ and 28° data are shown in Fig. 5.13. In this case, the Λ peak comes out in exactly the right place, while the neutron peak is shifted lower than its true value. In the $\theta_{SOS} = 28°$ spectrum a small Σ^0 peak is also visible at $M_X^2 = 1.417$ GeV^2. The results of the peak fits using the π^+ and kaon masses are shown in Tables 5.5 and 5.6 respectively.

Table 5.4: M_X^2 calculated using the proton mass

Particle	M_X^2 from PDG	M_X^2 ($\theta_{SOS} = 53°$)	M_X^2 ($\theta_{SOS} = 40°$)
η	0.299	0.3015 ± 0.0021	0.3074 ± 0.0023
ω	0.616	-	0.6141 ± 0.0019

Table 5.5: M_X^2 calculated using the pion mass

Particle Peak	M_X^2 from PDG	M_X^2 ($\theta_{SOS} = 40°$)	M_X^2 ($\theta_{SOS} = 28°$)
neutron	0.8828	0.8844 ± 0.0005	0.8911 ± 0.0003
Λ	1.243	1.356 ± 0.006	1.334 ± 0.002

Table 5.6: M_X^2 calculated using the kaon mass

Particle Peak	M_X^2 from PDG	M_X^2 ($\theta_{SOS} = 40°$)	M_X^2 ($\theta_{SOS} = 28°$)
neutron	0.8828	0.8003 ± 0.0007	0.8279 ± 0.0003
Λ	1.243	1.245 ± 0.003	1.246 ± 0.001
Σ	1.416	-	1.417 ± 0.003

As a further check, the accidental and multi-pion backgrounds were subtracted from the data, which was then corrected for spectrometer acceptances and radiative effects to produce differential cross sections. These measured cross sections were then compared to the simulated cross section with good agreement [45], giving confidence that the spectrometer acceptances, target and beam calculations were well understood.

5.4.2 ω Photoproduction

The last five runs of the experiment were optimised for ω and ρ photoproduction off a 3% beryllium target. The same particle identification cuts as for the J/ψ analysis (section 5.2) were used to detect electrons and positrons from omega decay in the SOS and HMS respectively. The SOS was set to a central momentum of 0.9 GeV with angle 25°, while the HMS was set to a central momentum of 1.95 GeV and angle 11° (as shown in Table 4.4).

Fig. 5.14 shows the invariant mass spectrum of electron-positron coincidences from the decay of low mass vector mesons. Despite the very small branching ratios for $\omega \rightarrow e^-, e^+$ and $\rho \rightarrow e^-, e^+$, a clear peak at 785 MeV with a full width of 8 MeV corresponding to the ω is seen above a 140 MeV-wide ρ peak. Furthermore, the number of predicted ω events from a Monte Carlo simulation agreed with the number of observed events in the data. As a check on the reliability of the simulations with respect to the J/ψ results, the ω Monte Carlo was kept as similar as possible to the J/ψ Monte Carlo.

The results of the LH2 and Be runs indicate that the spectrometers' detector

systems were indeed functioning correctly during the experiment, and the Monte Carlo simulations with the Bremsstrahlung spectrum and spectrometer acceptances were well modeled. This indicates that, had J/ψ mesons been produced during the production runs according to our assumed cross section, we would have detected and seen them in the final analysis.

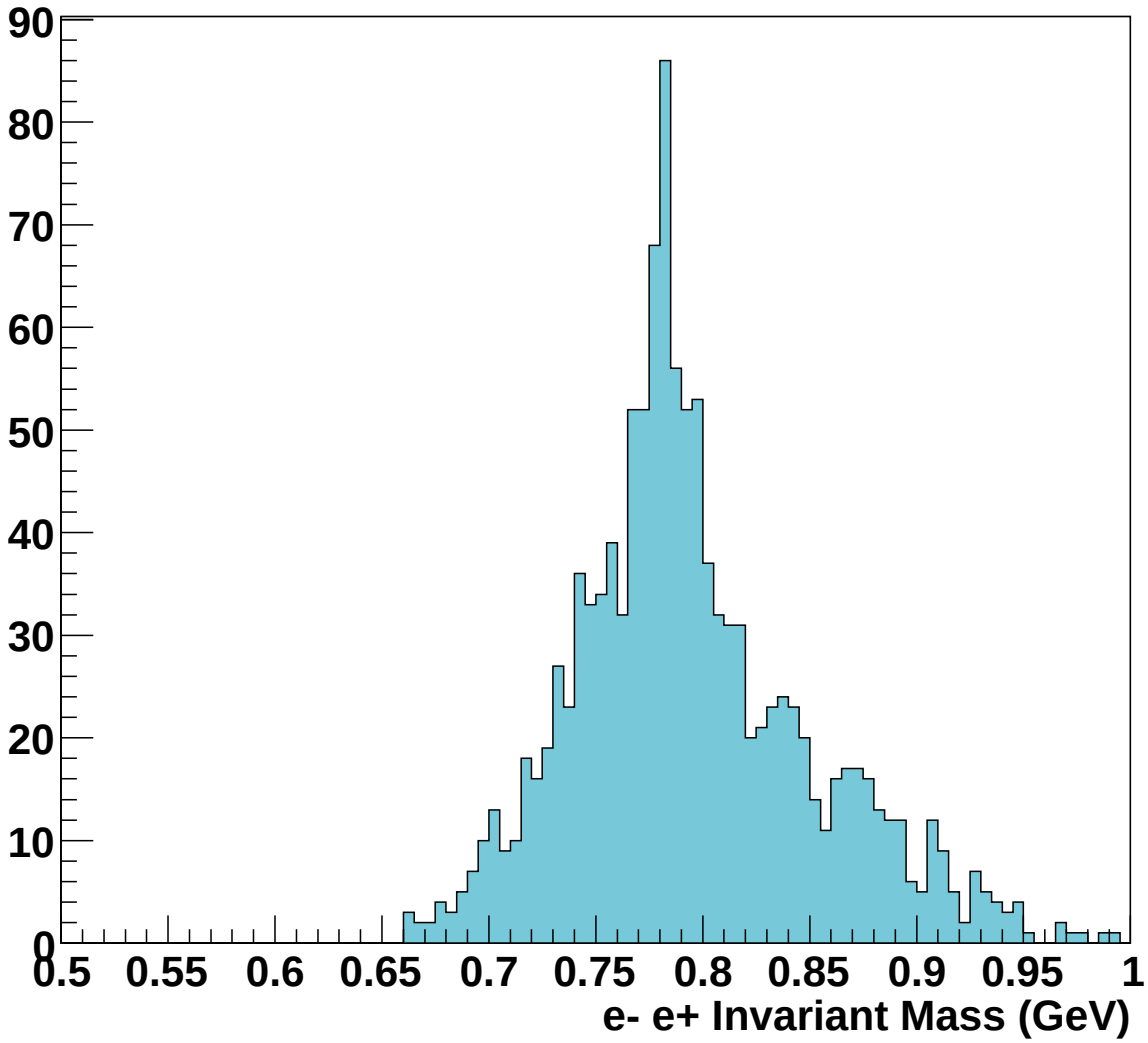

Figure 5.14: Reconstructed mass spectra for $\omega \rightarrow e^-, e^+$ and $\rho \rightarrow e^-, e^+$ coincidences.

Chapter 6

J/ψ Cross Section Analysis

Many experiments in nuclear and particle physics measure the cross section of a physical process by searching for events resulting from that particular process. In most cases the events are observed, and the cross section is determined as proportional to the number of those relevant events over the total running of the experiment.

In some experiments, however, the expected events are not observed. E03-008 was one such experiment: it was expected that a peak in the e^-e^+ mass spectrum at the J/ψ mass of 3.1 GeV would be seen; as the results in Fig. 5.8 show, no J/ψ events were detected. From the calibration runs it was determined that the detectors and data acquisition systems were working correctly, and our analysis codes were correct. So what, then, does this mean for the results of this experiment?

The lack of e^-e^+ and $\mu^-\mu^+$ events in the production runs does not necessarily mean that the J/ψ photoproduction process does not exist for a real

nucleus. For J/ψ production to occur a number of contributions are required (see Chapter 2.1): the photon has to fluctuate into a $c\overline{c}$ pair within the formation length of a nucleon; the nucleon has to contribute the necessary momentum to reach the invariant mass of the J/ψ; the J/ψ must decay into lepton pairs at the right momenta to be detected in the spectrometers; the list goes on, each of which can be the necessary culprit in preventing detection. Rather, then, the absence of dilepton events in the mass spectrum implies that the sub-threshold J/ψ photoproduction process is not seen at the level of sensitivity attained in E03-008.

Cross sections are typically quoted for particular photon energy (see Fig. 3.3). In this experiment, however, there is a folding of the internal momentum of the nucleons in the nucleus with the real photon energy (the real photon was not a monochromatic photon beam but a secondary bremsstrahlung beam), meaning that a simple upper limit value for the cross section cannot be extracted. Instead, we look at the count predictions various models give when under the same running conditions as the experiment. Here we can impose an upper limit on the number of counts predicted, based on our 87% confidence level observation of less than 2 counts (see appendix C).

6.1 J/ψ Acceptance

In any experiment the distribution of data obtained during the production runs does not map directly to the final data rate. For example, if the detectors covered only 20% of the total kinematics (and assuming the detector efficiencies were step functions) then the measured data rate for the experi-

ment would need to be multiplied by a factor of 5. This, of course, assumes that the process being measured is isotropic; if there was some angular or momentum dependence to the process however, the weighting factors would have to be considered proportionately.

For a fixed angle and momentum setting, the HMS and SOS spectrometers detect particles in a limited range around the central values. As the particles' kinematics deviate from these central values, the probability of detecting the particle decreases due to a variety of factors: hitting the collimator, scattering off internal detector elements, or missing important triggers. However, this detector efficiency is not necessarily symmetric about the central momentum and angle values. The consideration of the detector efficiencies combined with the geometric acceptances mentioned above give the total probability, or acceptance, for the process being measured.

To obtain the J/ψ acceptance for this experiment, we ran a Monte Carlo simulation creating particles of the J/ψ mass over a range of four-momenta P from 3.6 to 5.0 GeV and angle θ from 0° to 8°. The simulated J/ψ's were then decayed into lepton pairs with a 50% relative branching ratio to e^-e^+ and $\mu^-\mu^+$ pairs, and a $1 + \cos^2\theta_{CM}$ dependance on the center of mass angle [46]. The ranges for P and θ were chosen such that the lepton pairs resulting from the decay were within the correct kinematic range to make it into the spectrometers. The resulting set of four-momentum vectors of the lepton pairs were then run through the Jefferson Lab Hall C in-house detector simulation package [47], accurately modeling the acceptance of the

HMS and SOS spectrometers at the same kinematic settings as for E03-008.

The results of the Monte Carlo represent a calculation of the proportion of J/ψ's decaying to lepton pairs that made it through the detector as a function of J/ψ momentum and angle, and are shown in Table 6.1. It is clear from the table that for J/ψ momenta between 4 and 4.5 GeV, and with very forward angles ($\theta \leq 4^\circ$) the detector efficiency is greater than 1×10^{-4}.

6.2 J/ψ Cross Section Model Predictions

As discussed in section 3.3, using the following integral to model quasi-free J/ψ photoproduction from a heavy nucleus

$$d\sigma = \int \Phi(k)dk \int \frac{d\sigma_0(s,t)}{dt}\, \alpha_{LC}(P_m, E_m) S(E_m, \vec{P}_m) d^3\vec{P}_m dE_m dt \qquad (6.1)$$

we are left with the free nucleon cross section $d\sigma_0(s,t)/dt$ and the carbon spectral function $S(E_m, \vec{P}_m)$ of Benhar [30] at high $\vec{P}_m$ and E_m as our two unknowns. Beyond $P_m = 0.6$ GeV there is insufficient data to constrain the function, so we apply four different choices to extend the spectral function above this value. First, two extrapolations of the nucleon momentum probability distribution integrated over E_m were made, hereafter referred to as "high" or "low" depending on whether they are higher or lower at large P_m (as discussed in [6], the "high" extrapolation is more like an upper bound and will thus probably overestimate the yields). Then, two choices are used for the E_m distribution: either "freeze" the value to that of Benhar et al. at $P_m = 0.8$ GeV [30], or shift the distribution by $\sqrt{m^2 + P_m^2} - \sqrt{m^2 + 0.8^2}$, (where P_m is in units of GeV).

Table 6.1: Probability ($\times 10^{-4}$) of detecting a J/ψ with momentum P and angle θ.

	$\theta^{\rm Lab}_{J/\psi}$									
P(GeV)	$0-0.8^\circ$	$0.8-1.6^\circ$	$1.6-2.4^\circ$	$2.4-3.2^\circ$	$3.2-4.0^\circ$	$4.0-4.8^\circ$	$4.8-5.6^\circ$	$5.6-6.4^\circ$	$6.4-7.2^\circ$	$7.2-8.0^\circ$
3.60 - 3.74	0.000	0.000	0.000	0.000	0.000	0.000	0.000	0.000	0.000	0.000
3.74 - 3.88	0.000	0.000	0.020	0.040	0.000	0.020	0.040	0.000	0.000	0.000
3.88 - 4.02	0.780	0.581	0.840	0.762	0.441	0.300	0.240	0.080	0.000	0.000
4.02 - 4.16	3.448	3.177	2.760	2.420	1.722	1.020	0.420	0.260	0.120	0.000
4.16 - 4.30	6.170	5.804	5.166	4.468	1.860	0.979	0.440	0.020	0.000	0.000
4.30 - 4.44	4.780	4.402	3.943	3.379	2.434	0.919	0.480	0.120	0.020	0.000
4.44 - 4.58	1.900	2.223	2.262	2.101	1.643	1.299	0.740	0.160	0.040	0.000
4.58 - 4.72	0.080	0.260	0.519	0.638	0.821	0.481	0.260	0.160	0.000	0.000
4.72 - 4.86	0.000	0.000	0.040	0.040	0.060	0.020	0.020	0.000	0.000	0.000
4.86 - 5.00	0.000	0.000	0.000	0.000	0.000	0.000	0.000	0.000	0.000	0.000

Following the discussion in section 3.2, we used three different models for the free nucleon cross section:

$$\text{I. } \frac{d\sigma_0}{dt} = Ae^{bt} \tag{6.2}$$

$$\text{II. } \frac{d\sigma_0}{dt} = A\frac{1}{(1-bt)^4} \tag{6.3}$$

$$\text{III. } \frac{d\sigma_0}{dt} = A\frac{(1-x)^2}{(1-bt)^4} \tag{6.4}$$

where $x = \frac{2mM_{J/\psi}+M_{J/\psi}^2}{s-m^2}$ and A and b are free parameters. Model I uses the form factor from the SLAC [20] and Cornell [22] fits, and models II and III use the dipole form factor of [24] in the three- and two-gluon exchange models of [1] respectively.

To test the validity of each of the models, the number of counts predicted by each model was calculated as a function of the t-slope parameter b within the range 0 to 3 GeV^{-2}. The relative rate for the experiment was calculated for a total of four days of production running on a beam current of 80 μA, taking into account the specifics of target radiation length and thickness and weighted by the Bremsstrahlung distribution $\frac{1}{k}$ and a 12% branching ratio (6% each for $J/\psi \rightarrow e^+e^-$ and $\mu^+\mu^-$). This was then scaled by the detection probability given in the acceptance table above, and used to standardise the predictions made by the models to the conditions of the experiment. A was calculated for each value of b such that the curves would agree with the Cornell cross section measurement of 0.7 nb at an incident photon energy of $k = 11$ GeV [22].

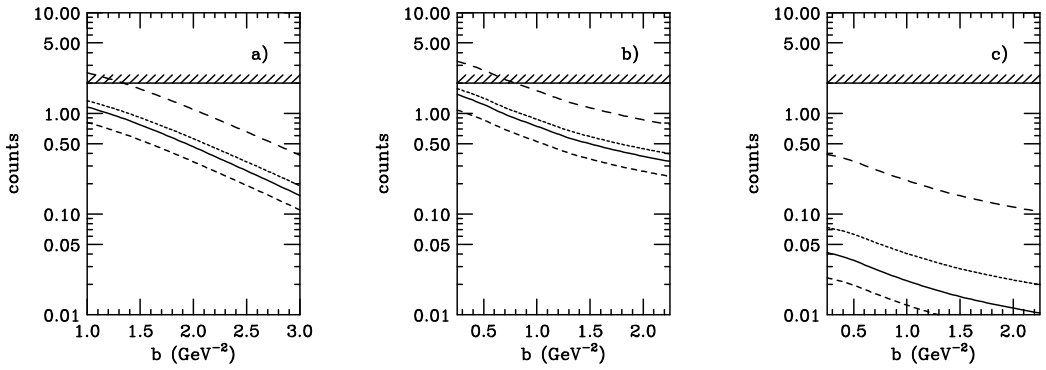

Figure 6.1: The number of predicted counts for the conditions of the present experiment as a function of b for: a) Model I; b) Model II; and c) Model III, where the models are defined in Equations 6.2, 6.3, and 6.4, respectively. On each panel, the solid (long dashed) curves use the "high" extrapolation of the spectral function with (without) the E_m shift for $P_m > 0.8$ GeV described in the text. The medium dashed (short dashed) are the corresponding curves with the "low" extrapolation. The hatched band at 2 counts indicates the 87% confidence level corresponding to our experimental observation of no events.

Figs. 6.1a, b and c show the number of events expected for this experiment as predicted by models I, II, and III respectively, for the four high-P_m extrapolations of the spectral function. For all three models, shifting the E_m distributions for $P_m > 0.8$ results in a difference in the predicted rates of about a factor of two. The predicted rates for model III are lower than for models I and II because of the stronger s dependence due to the extra factor of $(1-x)^2$. The sensitivity to the various extrapolations of the spectral function is also largest for model III, because on average higher values of P_m are probed.

The restriction placed on the models was that they had to predict fewer than the 2 counts allowed by the 87% confidence level on the experiment (see appendix C), over all values of b, shown by the hashed lines in Fig. 6.1. As can be seen in the plots, all combinations of the three models satisfy this requirement. However, it may be possible that something like the "hot spot" scenario discussed in section 2.3 could occur, resulting in predictions greater than two counts, especially for models I and II. This could correspond, in the quasi-free picture, to considerably lower values of E_m than in the Benhar spectral function used above.

As mentioned in section 3.1, we can use the calculations of charm ($c\bar{c}$) photoproduction rates by Braun and Vlahovic [23] as a guide. Assuming domination of the pQCD simple photon-gluon fusion process, their calculation predicts a total cross section of about 0.25 fb/nucleon for carbon with 5.5 GeV photons, corresponding to approximately 0.02 events under our experimental conditions, similar to our predictions using Model III.

Chapter 7

Conclusion

E03:008 aimed to measure the cross section for sub-threshold J/ψ photoproduction on a solid carbon target. No J/ψ events were observed, consistent with predictions of quasi-free production using three elementary models for free nucleon cross section, and reasonable extrapolations for the high missing momentum and energy spectral function distributions in carbon. Due to the non-observation of J/ψ's, extensive consistency checks were done using liquid hydrogen and beryllium targets to ensure the detectors and Monte Carlo simulators were functioning correctly. The checks showed nucleon resonances from electron-proton scattering as well as leptonic decays from ω photoproduction, evidencing the experimental apparatus was functioning and configured correctly and analytic procedures were robust, and thus giving a high level of confidence that the null result was real.

It was seen that the predictions given by the models did vary slightly amongst themselves, and the rates were also sensitive to the different extrapolation methods for the spectral function. All models, however, satisfied the re-

quirement of predictions in line with our 87% confidence level observation of less than 2 counts. The non-observation of J/ψ photoproduction seems to indicate that unusual high momentum components in the nucleus are unlikely. Therefore, for a given set of assumptions on the choice of carbon spectral function, and the parametrization of the free nucleon cross section near threshold, upper limits could be set on exotic mechanisms such as gluon exchange to two different nucleons, hidden colour configurations, "hot spot" scenarios, etc, that may enhance the sub-threshold cross sections.

For further analysis of the J/ψ photoproduction cross section and interpretation of the present experiment's results it will be important to have well-characterised spectral functions and precision measurements of the free nucleon cross section in the 8-11 GeV region. This will be possible with the 11 GeV upgrade at Jefferson Lab, and an experiment is already planned [9] to provide definitive measurements of J/ψ photoproduction on hydrogen in the near threshold region. This experiment will place further constraints on the photoproduction models and provide better knowledge of the A-dependence of the photoproduction cross section. With this future experiment the proposal authors expect a factor of three improvement on the determination of the J/ψ-nucleon total scattering cross section, a fundamental quantity that is calculable in specific models. Furthermore, this will be measured at a center-of-mass energy of 5 GeV, in the range of interest for studies of the quark-gluon plasma and of importance in the interpretation of J/ψ suppression in heavy ion collisions.

Appendix A

E/P Peak Positions on Calorimeter

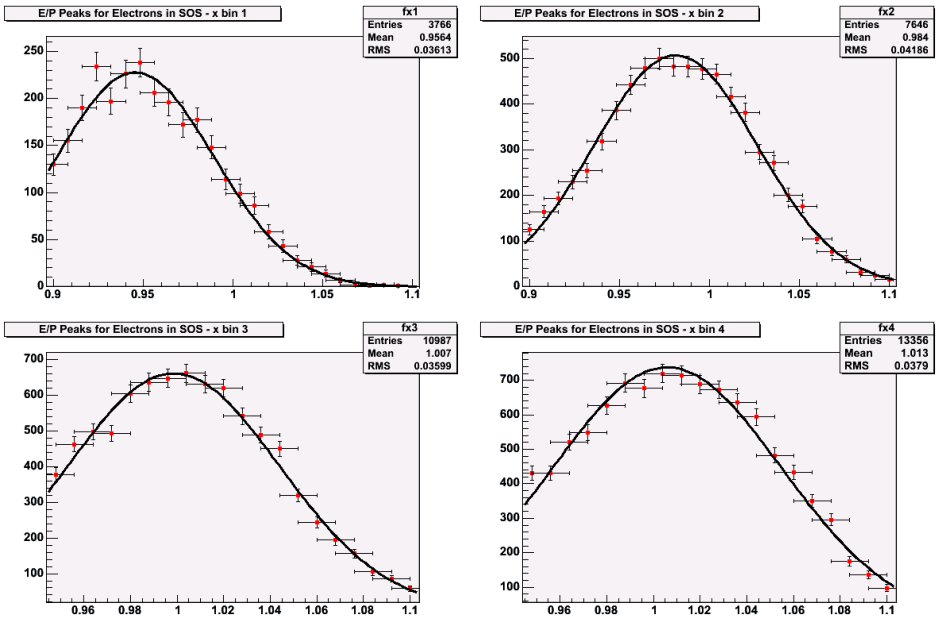

Figure A.1: Electron E/p peaks over all runs for different positions on the x-axis of the SOS calorimeter

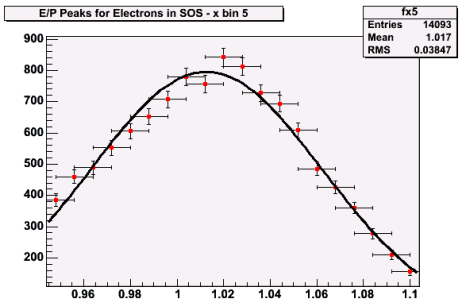
E/P Peaks for Electrons in SOS - x bin 5
fx5
Entries 14093
Mean 1.017
RMS 0.03847

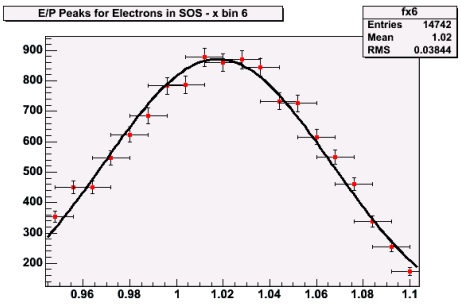
E/P Peaks for Electrons in SOS - x bin 6
fx6
Entries 14742
Mean 1.02
RMS 0.03844

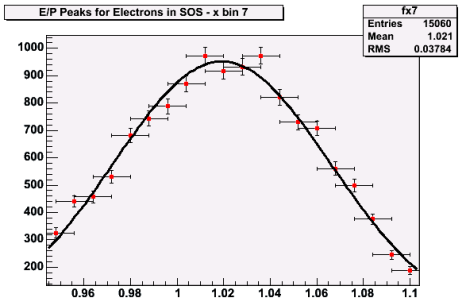
E/P Peaks for Electrons in SOS - x bin 7
fx7
Entries 15060
Mean 1.021
RMS 0.03784

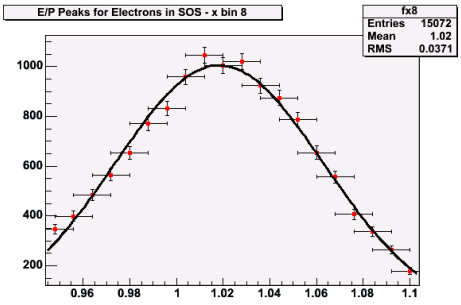
E/P Peaks for Electrons in SOS - x bin 8
fx8
Entries 15072
Mean 1.02
RMS 0.0371

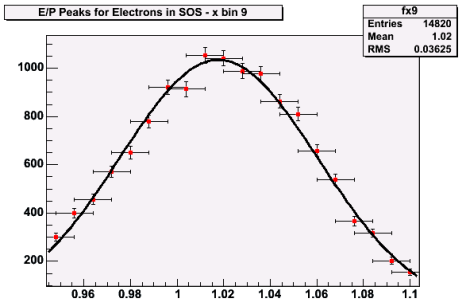
E/P Peaks for Electrons in SOS - x bin 9
fx9
Entries 14820
Mean 1.02
RMS 0.03625

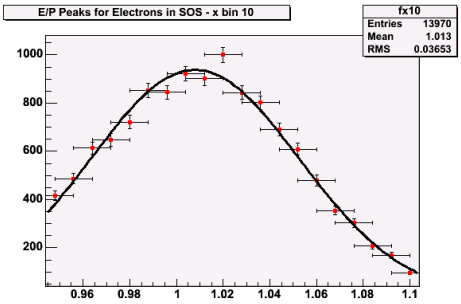
E/P Peaks for Electrons in SOS - x bin 10
fx10
Entries 13970
Mean 1.013
RMS 0.03653

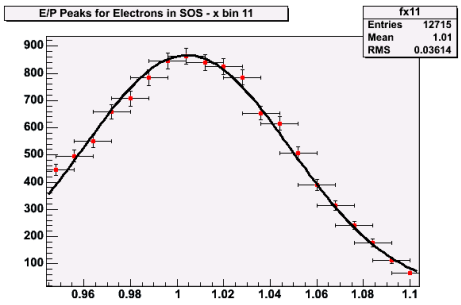
E/P Peaks for Electrons in SOS - x bin 11
fx11
Entries 12715
Mean 1.01
RMS 0.03614

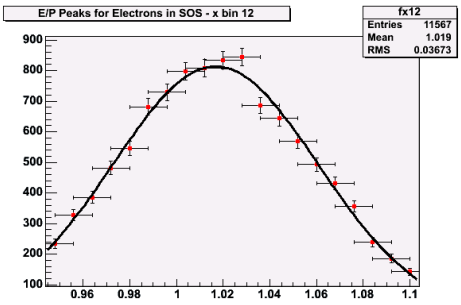
E/P Peaks for Electrons in SOS - x bin 12
fx12
Entries 11567
Mean 1.019
RMS 0.03673

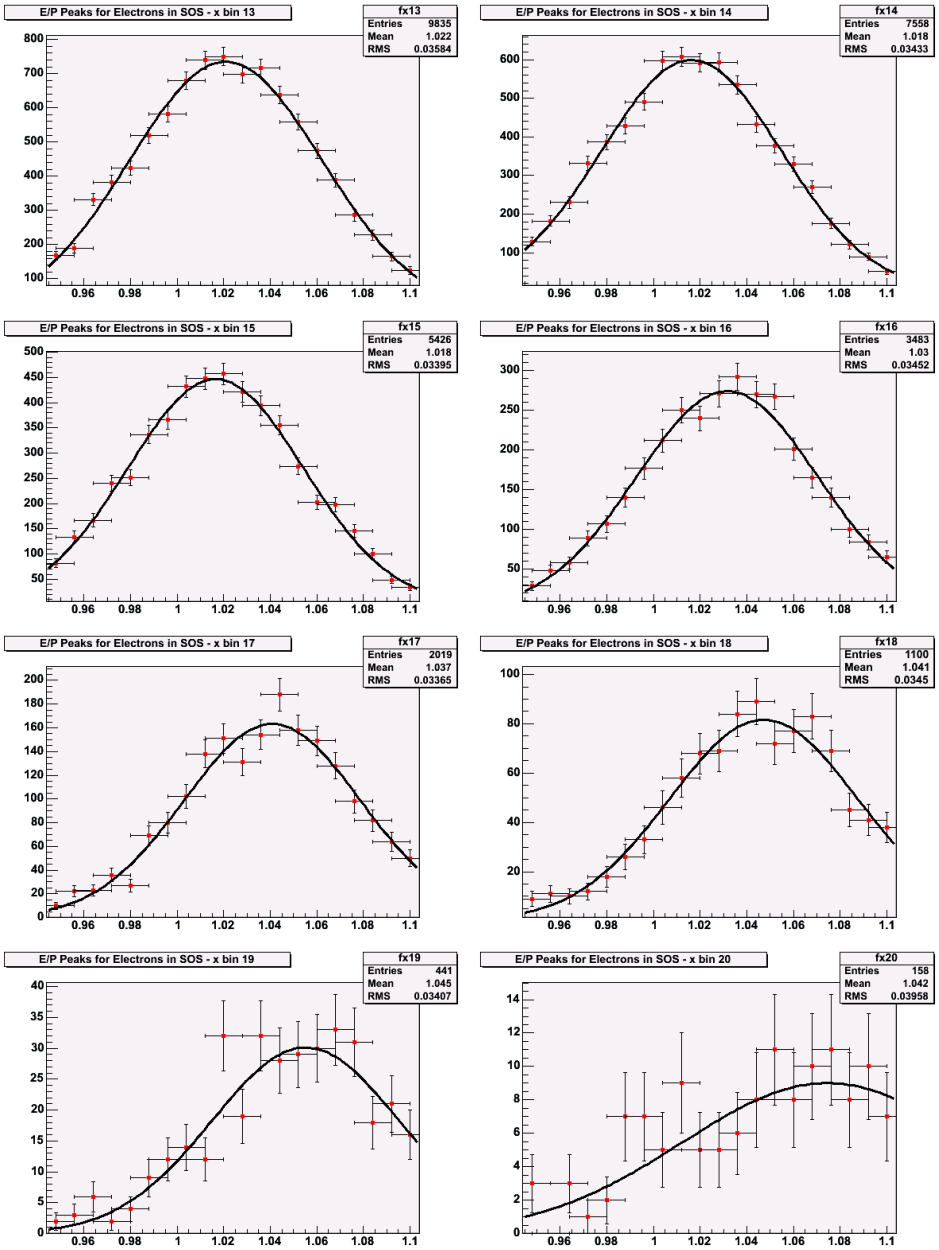
E/P Peaks for Electrons in SOS - x bin 13
fx13
Entries 9835
Mean 1.022
RMS 0.03584
E/P Peaks for Electrons in SOS - x bin 14
fx14
Entries 7558
Mean 1.018
RMS 0.03433
E/P Peaks for Electrons in SOS - x bin 15
fx15
Entries 5426
Mean 1.018
RMS 0.03395
E/P Peaks for Electrons in SOS - x bin 16
fx16
Entries 3483
Mean 1.03
RMS 0.03452
E/P Peaks for Electrons in SOS - x bin 17
fx17
Entries 2019
Mean 1.037
RMS 0.03365
E/P Peaks for Electrons in SOS - x bin 18
fx18
Entries 1100
Mean 1.041
RMS 0.0345
E/P Peaks for Electrons in SOS - x bin 19
fx19
Entries 441
Mean 1.045
RMS 0.03407
E/P Peaks for Electrons in SOS - x bin 20
fx20
Entries 158
Mean 1.042
RMS 0.03958

Appendix B

LH2 Missing Mass Fits

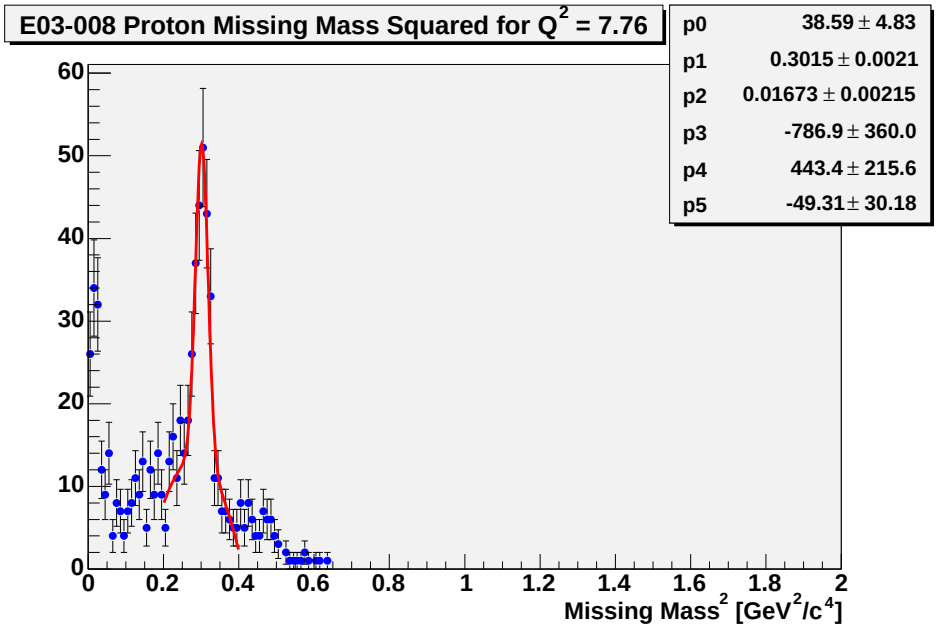

Figure B.1: M_X^2 calculated with proton mass. Fit to η peak.

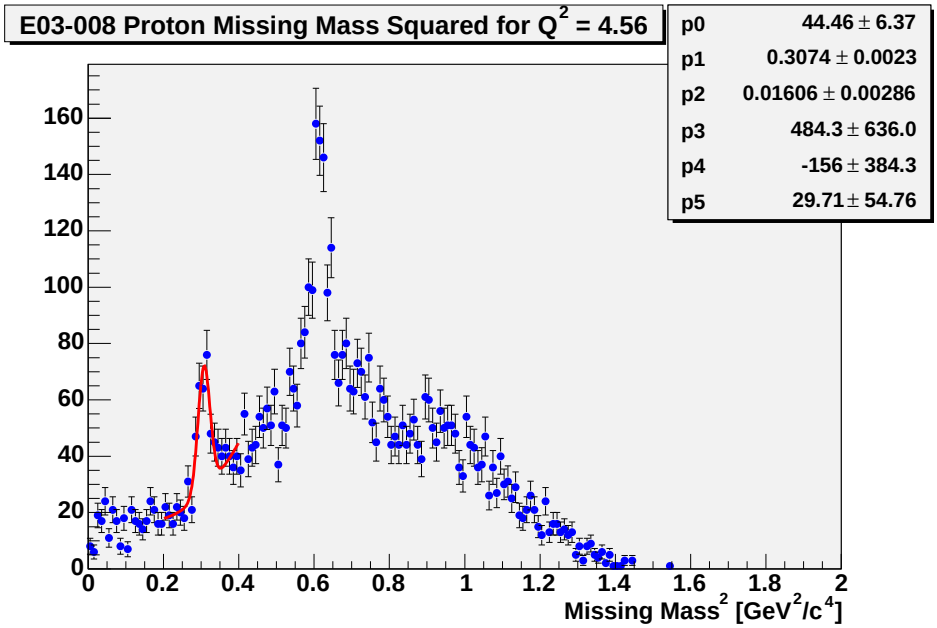

Figure B.2: M_X^2 calculated with proton mass. Fit to η peak.

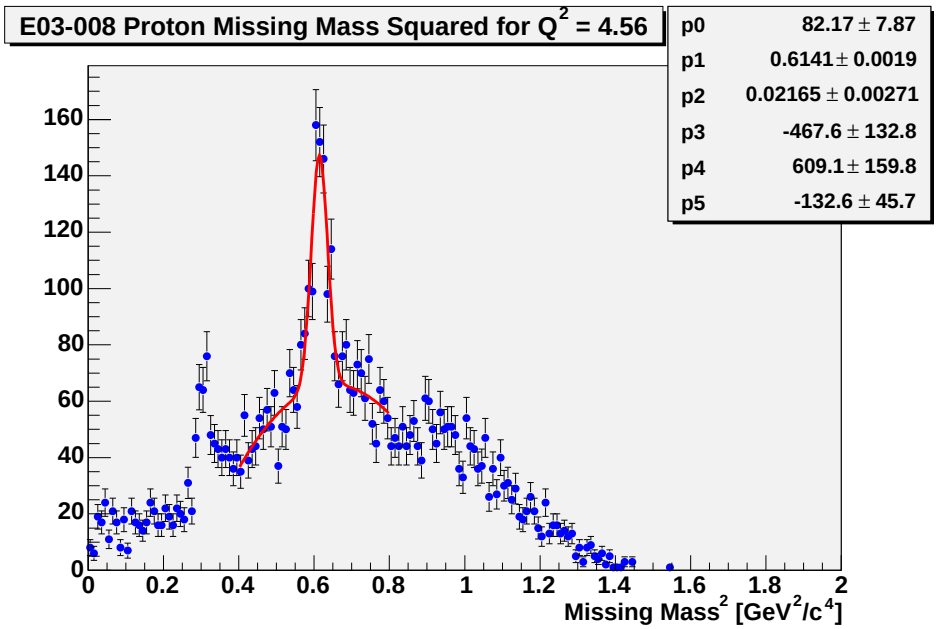

Figure B.3: M_X^2 calculated with proton mass. Fit to ω peak.

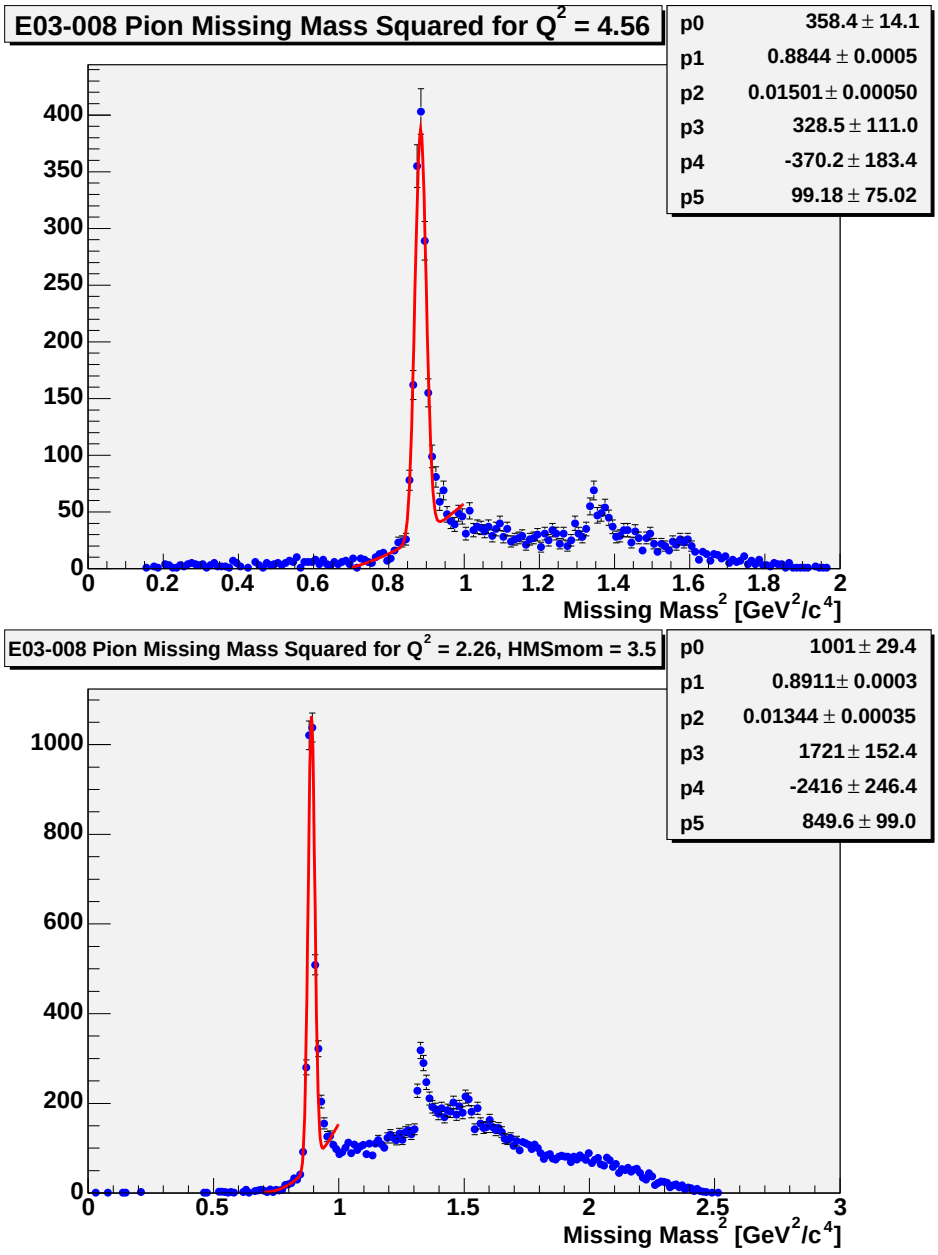

Figure B.4: M_X^2 calculated with pion mass. Fit to N peak.

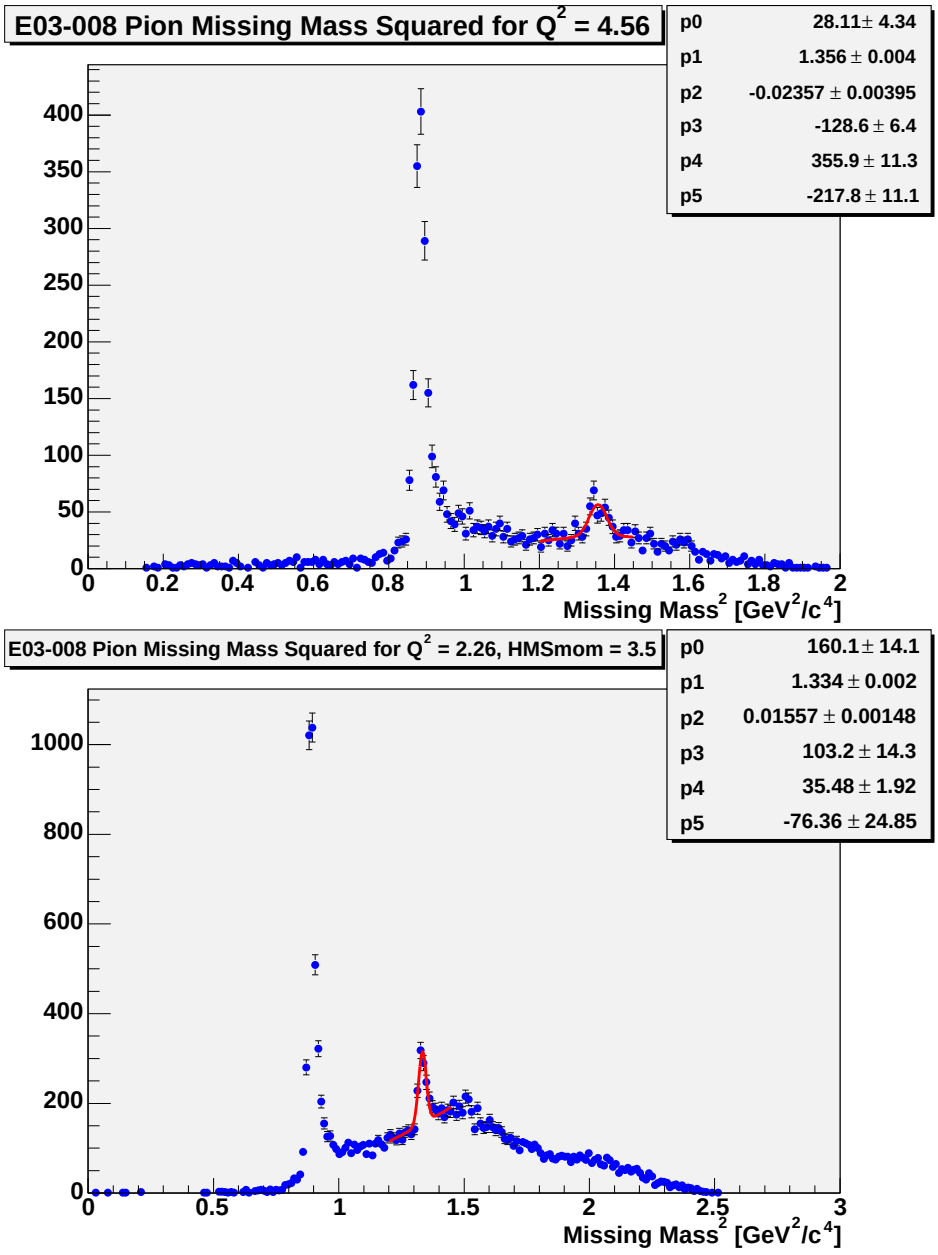

Figure B.5: M_X^2 calculated with pion mass. Fit to Λ peak.

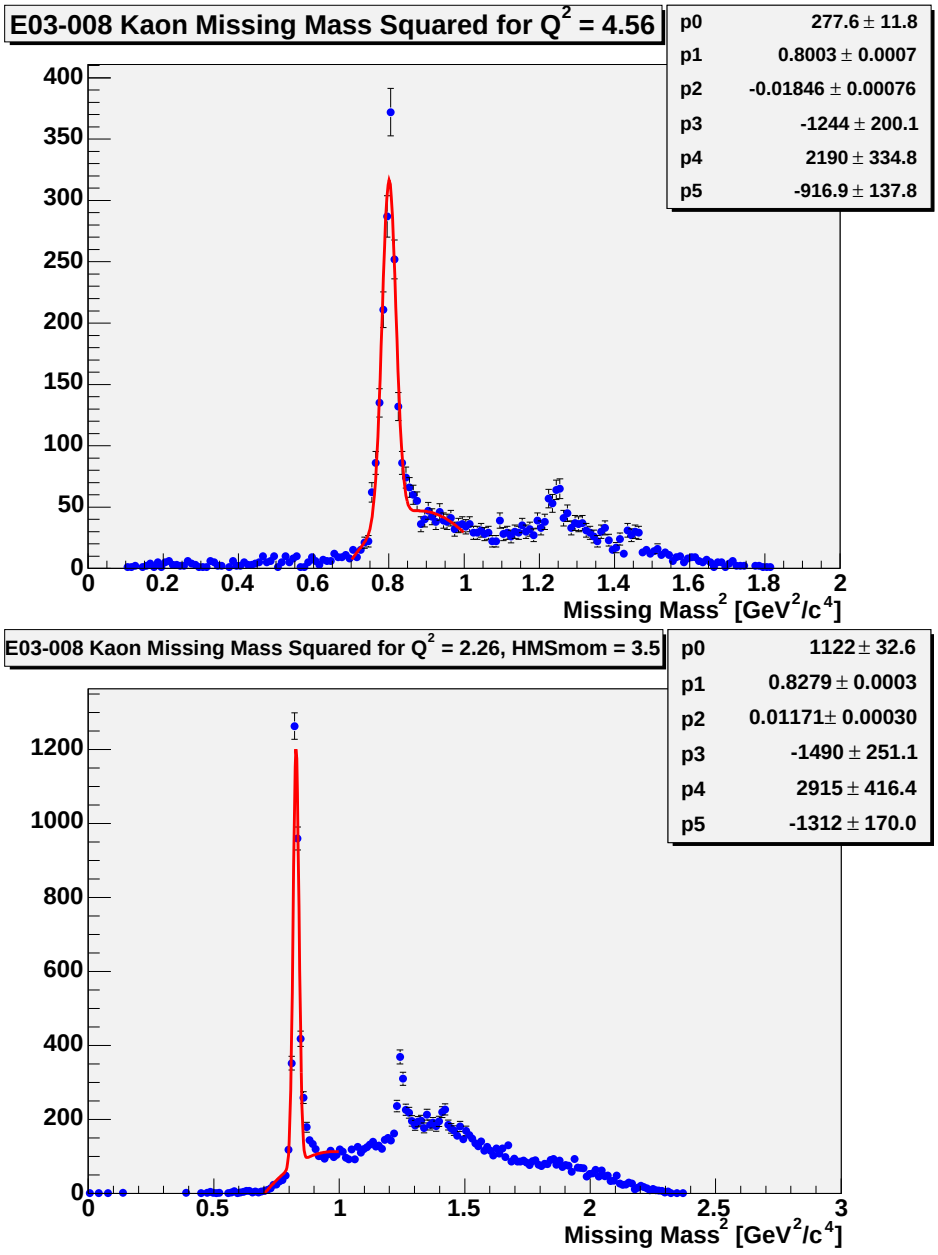

Figure B.6: M_X^2 calculated with kaon mass. Fit to N peak.

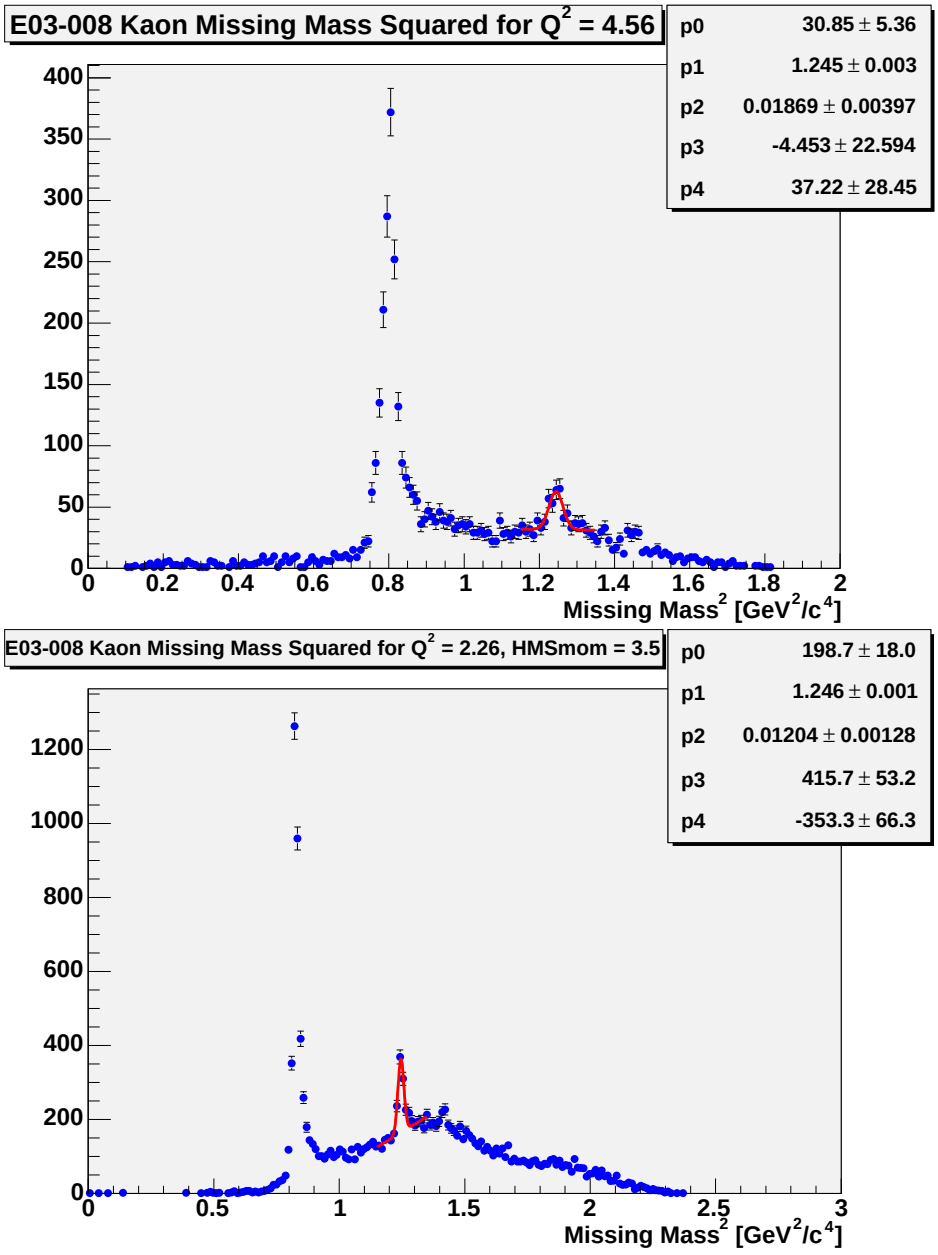

Figure B.7: M_X^2 calculated with kaon mass. Fit to Λ peak.

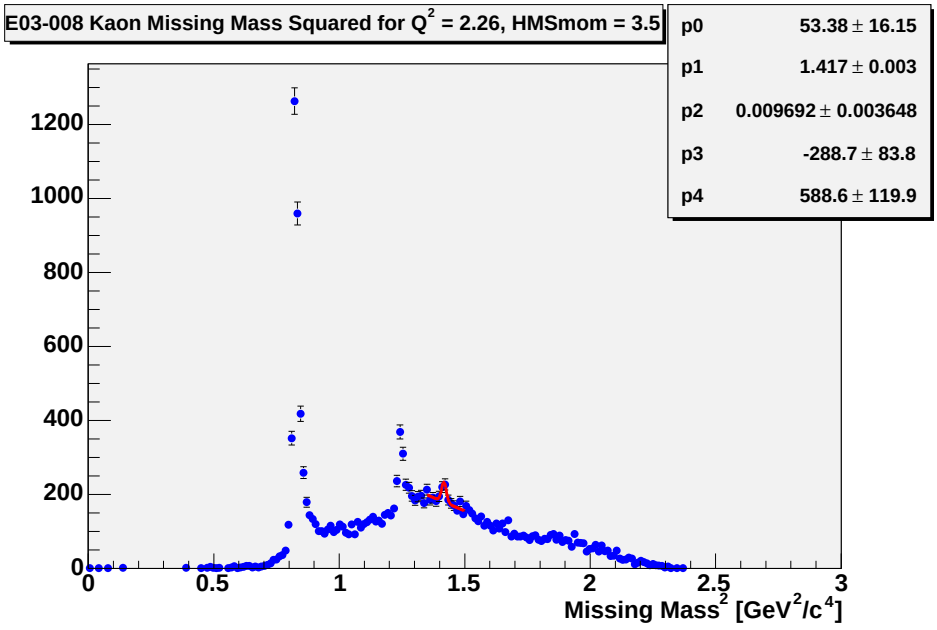

Figure B.8: M_X^2 calculated with kaon mass. Fit to Σ peak.

Appendix C

Count Limits

Since no J/ψ events were observed during the period of running of the experiment, we can write the probability that the reaction rate λ is less than some given rate λ_0 as [34]:

$$\text{prob}(\lambda < \lambda_0) = \int_0^{\lambda_0} Te^{-\lambda T} d\lambda = 1 - e^{-\lambda_0 T} \tag{C.1}$$

where the probability is normalised by the period T. This probability is also known as the confidence level (CL) for this process having a rate less than λ_0. We can thus write the rate λ_0 as:

$$\lambda_0 = -\frac{1}{T}\ln(1 - \text{CL}) \tag{C.2}$$

Multiplying both sides by T, we obtain an expression for the maximum number of counts allowed by model predictions for this experiment. Thus, assuming an upper limit of 2 counts, we obtain a confidence level of 87%:

$$\text{counts} = T\lambda_0 = 2 = -\ln(1 - \text{CL}) \Rightarrow \text{ CL} = 87\% \tag{C.3}$$

Appendix D

Publications

The results of Jefferson Lab experiment E03-008 have been published in the following paper:

1. Search for Sub-threshold Photoproduction of J/Psi Mesons, *Phys. Rev. C* **79**, (2009). P. Bosted, J. Dunne, C.A. Lee *et. al.*

The following publications arise from experiments at Jefferson Lab on which the author of this dissertation is a co-author (nee Gray):

1. Measurement of Nuclear Transparency for the A(e, e' π^+) Reaction, *Phys. Rev. Lett.* **99**, (2007). B. Clasie *et. al.*

2. Scaling Study of the Pion Electroproduction Cross Sections and the Pion Form Factor, *Phys. Rev. C* **78**, (2008). T. Horn *et. al.*

3. New Measurements of the EMC Effect in Very Light Nuclei, *in preparation for Phys. Rev. Lett.* J. Seely *et. al.*

Bibliography

[1] S. Brodsky, E. Chudakov, P. Hoyer, and J. Laget. Photoproduction of charm near threshold. *Phys. Lett.*, B498:23, 2001.

[2] Paul Hoyer. Physics at ELFE. *Nucl. Phys.*, A622:284c–314c, 1997.

[3] Stanley J. Brodsky, Paul Hoyer, Alfred H. Mueller, and Wai-Keung Tang. New QCD production mechanisms for hard processes at large x. *Nucl. Phys.*, B369:519–542, 1992.

[4] G. R. Farrar, L. L. Frankfurt, M. I. Strikman, and H. Liu. Color transparency and charmonium photoproduction. *Phys. Rev. Lett.*, 64:2996–2998, 1990.

[5] B. Z. Kopeliovich and B. G. Zakharov. Quantum effects and color transparency in charmonium photoproduction on nuclei. *Phys. Rev.*, D44:3466–3472, 1991.

[6] O. Benhar, S. Fantoni, and G. I. Lykasov. On the behaviour of the nuclear spectral function at high momentum and removal energy. *Eur. Phys. J.*, A5:137–141, 1999.

[7] L. L. Frankfurt and M. I. Strikman. Hard Nuclear Processes and Microscopic Nuclear Structure. *Phys. Rept.*, 160:235–427, 1988.

[8] E. Chudakov et al. Charm photoproduction near threshold. JLAB-TN-01-007 (Proposal).

[9] E.A. Chudakov, P. Bosted, and J.A. Dunne. Measuring of A-dependence of j/ψ photoproduction near threshold. 2007. JLAB PR12-07-106.

[10] Victor A. Matveev and Paul Sorba. Is Deuteron a Six Quark System? *Nuovo Cim. Lett.*, 20:435, 1977.

[11] Victor A. Matveev and Paul Sorba. Quark Analysis of Multi - Baryonic Systems. *Nuovo Cim.*, A45:257, 1978.

[12] Stanley J. Brodsky, Chueng-Ryong Ji, and G. Peter Lepage. Quantum Chromodynamic Predictions for the Deuteron Form- Factor. *Phys. Rev. Lett.*, 51:83, 1983.

[13] J. M. Laget and R. Mendez-Galain. Exclusive photoproduction and electroproduction of vector mesons at large momentum transfer. *Nucl. Phys.*, A581:397–428, 1995.

[14] Stanley J. Brodsky and John R. Hiller. Reduced Nuclear Amplitudes in Quantum Chromodynamics. *Phys. Rev.*, C28:475, 1983.

[15] A. Shor et al. Subthreshold anti-proton, K-, K+ and energetic pion production in relativistic nucleus-nucleus collisions. *Phys. Rev. Lett.*, 63:2192–2195, 1989.

[16] J. B. Carroll et al. Subthreshold anti-proton production in Si-28 + Si-28 collisions at 2.1 GeV/nucleon. *Phys. Rev. Lett.*, 62:1829–1932, 1989.

[17] A. A. Baldin et al. Anti-proton yeild in collision of carbon nuclei with copper nuclei at energy of 3.65 GeV/nucleon. *JETP Lett.*, 48:137–140, 1988.

[18] V.P. Koptev et. al. Subthreshold k+ meson production in proton-nucleus interactions. *Sov. Phys. JETP*, 1988.

[19] A. Shor, V. Perez-Mendez, and K. Ganezer. Internal nuclear momentum and subthreshold anti-proton production in p-nucleus and nucleus-nucleus collisions. *Nucl. Phys.*, A514:717–733, 1990.

[20] U. Camerini et al. Photoproduction of the ψ particles. *Phys. Rev. Lett.*, 35:483, 1975.

[21] *SLAC Summer Institute Lepton-Photon Symposium*, 1975.

[22] Gittelman et al. Photoproduction of the $\psi(3100)$ meson at 11 GeV. *Phys. Rev. Lett.*, 35:1616, 1975.

[23] M. Braun and B. Vlahovic. Estimates of the sub-threshold photoproduction of charm. *hep-ph*, 2002.

[24] L. Frankfurt and M. Strikman. Two-gluon form-factor of the nucleon and j/ψ photoproduction. *Phys. Rev.*, D66, 2002.

[25] S.J. Brodsky, M. Burkardt, and I. Schmidt. Qcd constraints on the shape of polarized quark and gluon distributions. *Nucl. Phys.*, B441:197–214, 1995.

[26] Edmond L. Berger and Stanley J. Brodsky. Quark Structure Functions of Mesons and the Drell-Yan Process. *Phys. Rev. Lett.*, 42:940–944, 1979.

[27] J. M. Laget. Photoproduction of vector mesons at large transfer. *Phys. Lett.*, B489:313–318, 2000.

[28] A. Donnachie and P. V. Landshoff. Dynamics of Elastic Scattering. *Nucl. Phys.*, B267:690, 1986.

[29] R. H. Dalitz and D. R. Yennie. Pion production in electron-proton collisions. *Phys. Rev.*, 105:1598–1615, 1957.

[30] O. Benhar, A. Fabrocini, S. Fantoni, and I. Sick. Spectral function of finite nuclei and scattering of GeV electrons. *Nucl. Phys.*, A579:493–517, 1994.

[31] L. L. Frankfurt and M. I. Strikman. On the Normalization of Nucleus Spectral Function and the EMC Effect. *Phys. Lett.*, B183:254, 1987.

[32] C.W. Leeman, D.R. Douglas, and G.A. Krafft. The continuous electron beam accelerator facility: Cebaf at the jefferson laboratory. *Ann. Rev. Nucl. Part. Sci.*, 51:413–450, 2001.

[33] H. Fenker. Particle Detectors: Tools of High Energy and Nuclear Physics. Talk, 2006.

[34] W. R. Leo. *Techniques for Nuclear and Particle Physics Experiments.* Springer-Verlag, 1987.

[35] C. Grupen. *Particle Detectors.* Cambridge University Press, 1996.

[36] R. Carlini et al. Hall C Operating Manual. Hall C Document, Thomas Jefferson National Accelerator Facility.

[37] L. Andivahis et al. Measurements of the electric and magnetic form-factors of the proton from Q**2 = 1.75-GeV/c**2 to 8.83-GeV/c**2. *Phys. Rev.*, D50:5491–5517, 1994.

[38] D.J. Abbott et al. The CODA system and its performance in the first online experiments at CEBAF. Proceedings of the 1995 IEEE Conference on Real-Time Computer Applications in Nuclear, Particle and Plasma Physics, May 1995.

[39] Yung-Su Tsai. Pair Production and Bremsstrahlung of Charged Leptons. *Rev. Mod. Phys.*, 46:815, 1974.

[40] Yung-Su Tsai. Pair Production and Bremsstrahlung of Charged Leptons. (Erratum). *Rev. Mod. Phys.*, 49:421–423, 1977.

[41] Rene Brun and Fons Rademakers. ROOT - An Object Oriented Data Analysis Framework. Proceedings AIHENP'96 Workshop, Lausanne, Sep 1996. and Nucl. Inst. and Meth. in Phys. Res. A 389 (1997) 81-86. See also http://root.cern.ch/.

[42] C. S. Armstrong. *Electroproduction of the S11(1535) Resonance at High Momentum Transfer*. PhD thesis, College of William and Mary, 1998.

[43] V. Frolov. *Electroproduction of the Δ(1232) Resonance at High Momentum Transfer*. PhD thesis, Rensselaer Polytechnic Institute, 1998.

[44] M.M. Dalton. *Baryon Resonance Electroproduction at High Momentum Transfer*. PhD thesis, University of the Witwatersrand, 2008.

[45] M.M. Dalton et al. Electroproduction of eta mesons in the s11(1535) resonance region at high momentum transfer. *arXiv:0804.3509v3*, 2008.

[46] K. Schilling, P. Seyboth, and Guenter E. Wolf. On the Analysis of Vector Meson Production by Polarized Photons. *Nucl. Phys.*, B15:397–412, 1970.

[47] J. Arrington. A-B-SIMC. Hall C In-House Publication, 2001.